DIPLOMARBEIT

Interband Cascade Infrared Photodetectors for High-speed Applications

zur Erlangung des akademischen Grades

Diplom-Ingenieurin

im Rahmen des Masterstudiums

Mikroelektronik und Photonik

unter der Leitung von

Betreuung: Assoc.-Prof. Dr. Benedikt Schwarz
Mitwirkung: Dr. Hedwig Maria Knötig
Institut für Festkörperelektronik

eingereicht an der

Technischen Universität Wien
Fakultät für Elektrotechnik und Informationstechnik

von

Anna Lardschneider, BSc.
Matrikelnummer 01326582

Wien, im November 2022

Anna Lardschneider

Eidesstattliche Erklärung

Hiermit erkläre ich, dass ich die vorliegende Arbeit gemäß dem Code of Conduct – Regeln zur Sicherung guter wissenschaftlicher Praxis, insbesondere ohne unzulässige Hilfe Dritter und ohne Benutzung anderer als der angegebenen Hilfsmittel, angefertigt wurde. Die aus anderen Quellen direkt oder indirekt übernommenen Daten und Konzepte sind unter Angabe der Quelle gekennzeichnet. Die Arbeit wurde bisher weder im In- noch im Ausland in gleicher oder in ähnlicher Form in anderen Prüfungsverfahren vorgelegt.

Wien,

Anna Lardschneider

Abstract

Interband cascade infrared photodetectors (ICIPs) are an emerging new class of photovoltaic mid-infrared detectors. They are based on optical interband transitions combined with fast carrier transport through an InAs/GaSb type-II superlattice (T2SL) absorber. The electrical and optical properties of the devices depend on their structure design, which can change in number of cascade stages, absorber thickness, doping as well as in an current-matched absorbers design. ICIPs feature a broad spectral bandwidth and high sensitivity, and are ideally suited for high-speed operations at room temperature. The focus of this thesis lies in the investigation of these interband cascade devices. A comparison between other well-performing mid-infrared detectors as the mercury cadmium telluride detector (MCT), quantum well infrared photodetector (QWIP), quantum cascade detector (QCD) and the ICIP is shown. However, the majority of the mid-infrared photodetectors research has been concentrated on how to improve quantum efficiency and decrease dark current in order to improve the detectivity (D*). The high-speed characteristics, as the 3-dB bandwidth performance of ICIPs are not yet fully studied. In this work, these characteristics are investigated and their limitations are analyzed. An optimized structure for the devices is elaborated and realized, reaching a 3-dB bandwidth of 1.95 GHz for an ICIP with 20 µm diameter operating under 5 V applied bias at room temperature. Finally, two high-speed applications are presented, such as free space optical communication and frequency comb spectroscopy, in which these fully-packaged ICIPs are implemented.

Kurzfassung

Interbandkaskaden-Infrarot-Photodetektoren (ICIPs) sind eine neue Klasse von photovoltaischen Detektoren im mittleren Infrarot Bereich. Ihr Funktionsprinzip basiert auf optischen Interbandübergangen in Kombination mit einem schnellen Ladungsträgertransport durch ein InAs/GaSb-Typ-II-Übergitterabsorber. Die elektrischen und optischen Eigenschaften des Bauelementes hängt vom Design der Struktur ab. Dabei beeinflussen die Anzahl der Kaskadenstufen, die Absorberdicke und die Dotierung sowie die Stromanpassung des Absorber das Verhalten des Detektors maßgeblich. ICIPs haben eine große spektrale Bandbreite sowie eine hohe Empfindlichkeit und sind deshalb ideal für den Hochgeschwindigkeitsbetrieb bei Raumtemperatur geeignet.

Der Fokus dieser Arbeit liegt in der Untersuchung dieser Interbandkaskaden Baudelemente. Dafür wird ein Vergleich zwischen anderen leistungsstarken Detektoren für das mittlere Infrarot wie zum Beispiel dem Quecksilber-Cadmium-Tellurid Detektor, dem Quantentopf-Infrarot-Photodetektor, dem Quantenkaskadendetektor mit dem ICIP präsentiert. Ein Großteil der Forschungsarbeit im Bereich der Photodetektoren konzentrierte sich bisher auf die Verbesserung der Quanteneffizienz und die Verringerung des Dunkelstroms um die Detektivität (D*) zu erhöhen. Die Hochgeschwindigkeitscharakteristika wie die 3-dB Bandbreite wurden bis jetzt noch nicht ausreichend erforscht. In dieser Arbeit wird gerade diese Eigenschaft untersucht und ihre Limitierungen analysiert. Eine optimierte Struktur für die ICIPs wird ausgearbeitet und realisiert. Dabei erreicht ein Bauelemt mit 20 µm Durchmesser und unter einer Vorspannung von 5 V eine 3-dB-Bandbreite von 1.95 GHz bei Raumtemperatur. Schlussendlich werden zwei aktuelle Hochgeschwindigkeitsanwendungen vorgestellt, in denen diese Detektoren bereits eingestzt wurden.

Acknowledgements

All good things come to an end, and so is also my time as a student. I am incredibly grateful for those who supported me on this rewarding and sometimes challenging journey. First, I want to thank Benedikt Schwarz for his guidance and support. Further thanks to all the invaluable professors and staff members at FKE, especially to Gottfried Strasser, Erich Gornik, Borislav Hinkov, Walter Weber, Hermann Detz, Masiar Sistani, Markus Schinnerl, Max Andrews, Anton Tsenov, Andreas Linzer, Christine Brendt and Werner Schrenk for their advice and assistance over the past few years.
I have been really lucky to work in a research group that consists of such fantastic members. First of all, I would like to thank Hedi for starting this journey at FKE with me and becoming a great supervisor and an amazing friend. Moreover, I particularly want to thank: Flo, for helping me in the lab and being a super fun and positive person with whom I am always happy to party; Sandro, for guiding me when needed from the step you are always ahead of me; Nikola, for offering me many back massages and a lot of wisdom. Mikołaj, for being such a cheerful person and always providing me with the newest sock trends. Andi, the newest group member that I actually know the longest, thank you for your help and enormous patience during my programming efforts; Miriam, for giving me great advice and the cutest coffee cups ever; Mauro, for many unforgettable pizza nights and for putting me on a paper's author list for the first time in my life; Elena, for being a genuinely good person whom I am grateful to call my friend. Stefi, for lots of great conversations, not only work related; Georg, for sharing his bike expertise and the offshoots of his plants with me. Thanks to anyone I did not mention but contributed to all of the great memories.

Thank you to Nina, Kerstin and Ale. Although each of us lives in a different place around the world, you are still such good friends to me, and for that, I am infinitely grateful.

Last, I want to thank my family. Mami, Tati I am forever grateful for your unconditional love and support and for letting me follow my dreams. This would not have been possible without you. Thanks, Lena, Jakob, Simona and Milla for being the way you are. Finally, thanks to all the rest of my family and friends. *-L'amour toujours-*

Contents

1 Introduction and Motivation

Infrared radiation was already discovered in the 19th century by William Herschel. However, the first infrared photodetectors were only invented in the late 20th century. Since then, the photodetection of infrared radiation has gained importance for various applications, and a large number of different detector concepts have been investigated, as seen in Fig. 1.1.
Generally, infrared radiation can be divided into four different classes. The shorter wavelength range form 0.8 - 3 µm is known as the near-wavelength infrared region (NWIR) and is of great importance for the telecommunication sector. The region from 3 - 5 µm is named mid-wavelength infrared region (MWIR) and the range from 8 - 12 µm is known as long-wavelength infrared region (LWIR). These regions are highly interesting for the gas spectroscopy since the majority of gaseous chemicals show characteristic absorption here. Finally, the very long-wavelength infrared region (VLWIR) is located above 14 µm [1]. The most beneficial spectral regions for chemical sensing, free-space communications and astronomy are the MWIR and LWIR, since low absorption windows of the terrestrial atmosphere are located precisely in these regions. Thus, transmission without significant losses, caused mainly by water vapour, is possible.

Nowadays, the most prominent photodetectors are based on technologies such as mercury cadmium telluride (MCT) and high-quality III-V material systems. However, significant research effort has been devoted to the improvement of the performance of infrared photodetectors over the past decade. Promising results were achieved recently with interband cascade infrared photodetectors (ICIPs) based on the interband cascade laser (ICL). ICIPs are feasible for high temperature and high-speed operation without compromises in detectivity. This leads to high-performance characteristics and low power consumption thanks to their high uniformity, reduced tunneling currents and suppressed Auger recombination. Moreover, thanks to their broad spectral bandwidth, they are emerging as a new type of detector for a broad variety of applications.

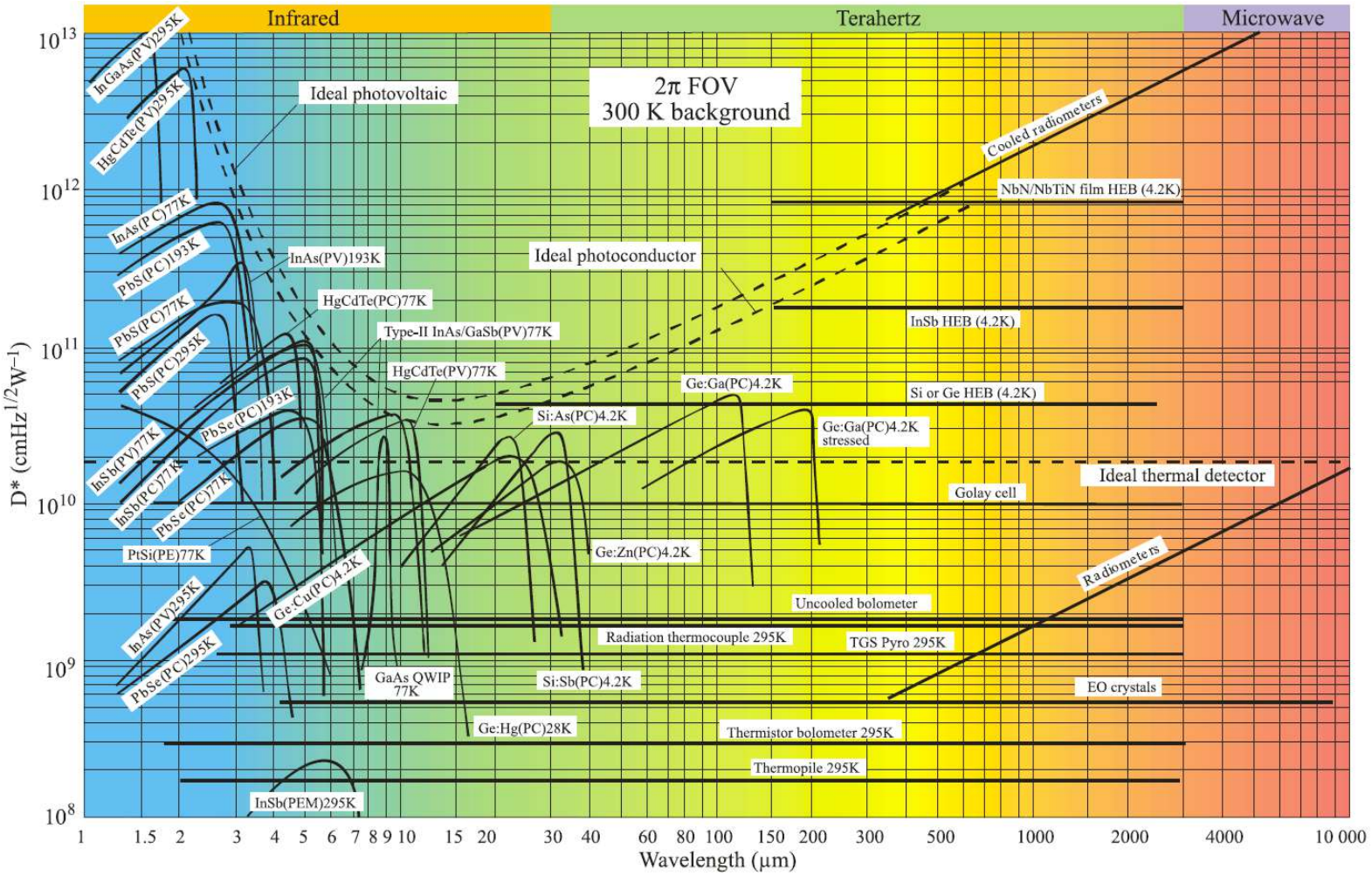

Figure 1.1: Comparison of the detectivity D* of various available detectors when operated at the indicated temperature. Theoretical curves for the background-limited D* (dashed lines) for ideal photovoltaic, ideal photoconductive and ideal thermal detectors are shown. Abbriviations: (HEB) Hot electron bolometer; (PC) Photoconductive detector; (PEM) Photoelectromagnetic detector; (PV) Photovoltaic detector. Figure taken from [2].

This thesis will shed light on the working principles, fabrication process and applications of ICIPs and was conducted based on the framework of the PhD thesis of H. Knötig [3]. The motivation for conducting research in this field was the need for high-speed detectors when studying frequency comb characteristics. Based on the results presented in the course of this work, also laser characterization, heterodyne detection and free-space optical communication experiments were performed with the realized ICIPs. Originating from the idea of producing faster detectors, the main focus of this work lies in the improvement of their high-frequency characteristics. The limitations of the devices were studied by employing varying superlattice absorber thicknesses and minimizing all parasitic electronic components.

Following this brief introduction, chapter 2 explains the general working principles of ICIPs. Moreover, the structure of the detectors is explained, and their limitations of the high-speed characteristics are discussed. Additionally, three different state-of-the-art detectors in the infrared are presented and compared to the ICIP. In chapter 3, the fabrication, starting from the MBE growth of the material to the finished devices is described. Also, a new design idea is proposed and all relevant processing steps for its implementation are explained. Chapter 4 describes the high-speed characteristics of the realized devices. The electrical and optical measurement setups and results are illustrated in this chapter. Furthermore, two high-speed applications in which these devices are being employed are presented. Chapter 5 concludes by considering the limitations of this study and suggesting further areas of research regarding this subject.

2 Mid-infrared photodetectors

This chapter gives a brief introduction of the fundamentals of ICIPs. A general overview of various state-of-the-art mid-infrared detectors is presented. Furthermore, the operating principle and the composition of an ICIP structure is explained in more detail. Finally, the electrical and optical limitations of the devices are discussed.

2.1 Theory

Band alignment:

The behavior of a semiconductor heterojunction depends strongly on the energy band alignment at the interface, of two different materials, and on the band offsets. The band offset can be described as the relative alignment of the band edge energies $E_i^{A,B}$ of two materials, A and B, at the Γ point [4]. These heterojunction interfaces can be divided into three categories, as seen in Fig.2.1. In type I alignment (straddling gap), the conduction band edge of material A is higher than in material B and the valence band edge of material A is lower compared to material B. Hence, in this composition, the interband transition is limited by the bandgap of material B. Next, in type II alignment (staggered gap), the conduction band edge of material B is in the bandgap of material A, while the valence band edge of material B is below the one of material A. Finally, in type II broken-gap, both the conduction band and valence band edge of material B are beneath the valence band edge of material A. Consequently, in such heterostructures, the energy of interband transition is not limited by the bandgap of material B. Hence, type II broken-gap quantum wells are ideally suited to construct interband optoelectronic devices at longer wavelengths. Table 2.1 gives an overview of the bandgap energy and the corresponding cutoff wavelength of different materials. A good example for a type II broken-gap alignments is a InAs/GaSb type II superlattice, where the valence band edge of a hole quantum well of GaSb (A) is energetically above the conduction band edge of an electron quantum well of InAs (B). Hence, the interband transition energy can simply be tuned by adjusting the structure of the InAs and GaSb quantum wells, reaching cutoff wavelengths ranging from 4 to 15 µm and beyond [5].

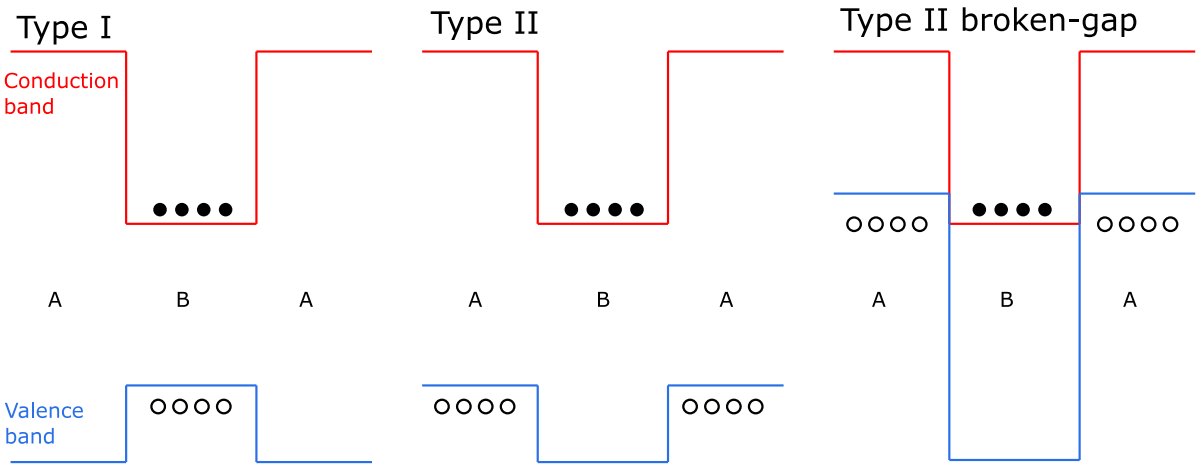

Figure 2.1: Semiconductor heterostructure with three different band alignments. Type II broken-gap quantum wells enable to build interband optoelectronic devices operating at longer wavelengths. The interband transition energy can simply be tuned by adjusting the width of the quantum wells. Figure adapted with permission from [4].

Material	Bandgap energy at 300K (eV)	Cutoff wavelength (μm)
Si (indirect)	1.12	1.1
Ge (indirect)	0.67	1.9
GaAs	1.43	0.9
InAs	0.35	3.5
InSb	0.17	7.3
$In_{0.53}Ga_{0.47}As$ (InP substrate)	0.73	1.7

Table 2.1: Overview of different bandgap energies with their corresponding cutoff wavelengths. The values of the III-IV materials were obtained from simulations of the material as lattice-matched to a InP substrate at 300K.

Optical interband transitions:

The following is a brief and very general description of all possible electronic transitions (interband and intersubband) that can lead to the absorption of a photon, adapted from [3, 6].

Optical interband transitions can be defined as an inelastic scattering process via photon absorption or emission. For sufficiently weak light fields, the interaction of electrons with optical fields can be described using perturbation theory and dipole approximation. An

incident photon can be absorbed and energetically lift an electron in the semiconductor from an occupied state to an unoccupied state. Consequently, the generated electron-hole pair can be described as an electric dipole. The Hamilonian in Eq.2.1 describes the interaction of the electric field $\vec{E}$ with the transition dipole moment $e\vec{r}$.

$$H_{ph} = e\vec{E} \cdot \vec{r} \tag{2.1}$$

The transition rate W_{if} between an initial state i and a final state f is given by Fermi's golden rule

$$W_{\mathrm{if}} = \frac{2\pi}{\hbar} |H_{ph}^{\mathrm{ij}}|^2 \delta(E_{\mathrm{i}} - E_{\mathrm{f}} - \hbar\omega), \tag{2.2}$$

with the interaction matrix element $\langle \mathrm{i}|H_{ph}|\mathrm{j}\rangle$. The only allowed transitions are those whose energy is equal to the energy difference from initial to final state $E_{\mathrm{i}} - E_{\mathrm{f}} = \hbar\omega$. This can be ensured by multpying the term with a Dirac δ-function.
Furthermore, a relation between the Hamiltonian H which describes the band structure (the eight-band Hamiltonian or any other arbitrary one) and the interaction matrix element $|H_{ph}|$ is derived. The dipole matrix element between two states φ_{ik} and φ_{fk} in the k-space can be rewritten in terms of the derivative of the Hamiltonian

$$\langle \varphi_{\mathrm{ik}}|\vec{r}|\varphi_{\mathrm{fk}}\rangle = -\frac{j}{(E_{\mathrm{fk}} - E_{\mathrm{ik}})} \langle \varphi_{\mathrm{ik}}|\nabla_{\mathrm{k}} H|\varphi_{\mathrm{fk}}\rangle \,. \tag{2.3}$$

Next, by inserting Eq.2.3 in the interaction Hamitonian of Eq. 2.1 it results in

$$H_{ph}^{ij} = \frac{eE_0}{2} \langle \varphi_{\mathrm{ik}}|\hat{e} \cdot \vec{r}|\varphi_{\mathrm{fk}}\rangle = -\frac{jeE_0}{2(E_{\mathrm{fk}} - E_{\mathrm{ik}})} \langle \varphi_{\mathrm{ik}}|\hat{e} \cdot \nabla_{\mathrm{k}} H|\varphi_{\mathrm{fk}}\rangle \,, \tag{2.4}$$

here, E_0 is the amplitude of the optical field and $\hat{e}$ denotes the axis along which the light is polarized. To describe the response of the medium to light, the optical susceptibility χ_{if} between an initial state i and final state f is given by

$$\chi_{\mathrm{if}} = \frac{e^2}{\epsilon_0} \sum_{\mathrm{k}} \frac{f_{\mathrm{fk}} - f_{\mathrm{ik}}}{(E_{\mathrm{fk}} - E_{\mathrm{ik}})^2} \frac{1}{\hbar\omega - (E_{\mathrm{fk}} - E_{\mathrm{ik}}) - j\gamma} |\sum_{\mathrm{m,n}} \langle \chi_{\mathrm{f,m}}|\hat{e} \cdot \nabla_{\mathrm{k}} H|\chi_{\mathrm{i,n}}\rangle|^2, \tag{2.5}$$

$\chi_{\mathrm{f,m}}$ and $\chi_{\mathrm{i,n}}$ in the matrix element are the coefficients of the envelope functions.
From the imaginary part of the susceptibility the absorption coefficient α can be derived,

$$\alpha(\omega) = -\frac{\omega}{n_r c_0} \operatorname{Im}\left\{ \sum_{\mathrm{i}} \sum_{\mathrm{f}>\mathrm{i}} \chi_{\mathrm{if}} \right\}, \tag{2.6}$$

n_r denotes the refractive index of the material and c_0 the vacuum speed of light. The absorption coefficient at a particular photon wavelength can be obtained from the sum over all possible transitions from initial to the final states. The second sum with index constraint f > i assures that the states are not counted twice.

Fast intraband transport:

The transport in an ICIP device can generally be described as a drift-diffusion process using Eq.2.7. J_n and J_p are the electron and hole current density, respectively, n is the carrier density for electrons and p for holes, q is the elementary charge and μ_n and μ_p are the carrier mobilities. $D_n = \frac{k_B T}{q}\mu_n$ and $D_p = \frac{k_B T}{q}\mu_p$ are the diffusion coefficients and E is the applied electric field.

$$\begin{aligned} J_n &= qn\mu_n E + qD_n \nabla n \\ J_p &= qp\mu_p E + qD_p \nabla p \end{aligned} \tag{2.7}$$

An illustration of the carrier transport in the superlattice is seen in Fig2.2. Here, interband tunneling through the miniband in the heterostructure region is assumed to occur on a timescale much faster than the generation-recombination processes. With no external field applied, a carrier has the same propability to subsequently tunnel to one of the adjacent quantum wells. The diffusion coefficient D of a superlattice absorber can approximately be expressed as indicated in Eq.2.8 [7].

$$D = \frac{(\Delta x_\omega)^2}{\tau_\omega} \qquad \rightarrow \qquad L = \sqrt{D\tau_{nr}} \tag{2.8}$$

τ_ω is the well-to-well transition time and Δx_ω is the length of a single superlattice period. Consequently, the carrier diffusion length L can be derived from this. Hence, by reducing the absorber thickness t below the diffusion length $t < L$, fast carrier transport is expected. When applying a external field, the probability of forward tunneling increases and the probability for backward tunneling is reduced, thus, carrier transport across the superlattice can reach the sub-picosecond timescale.

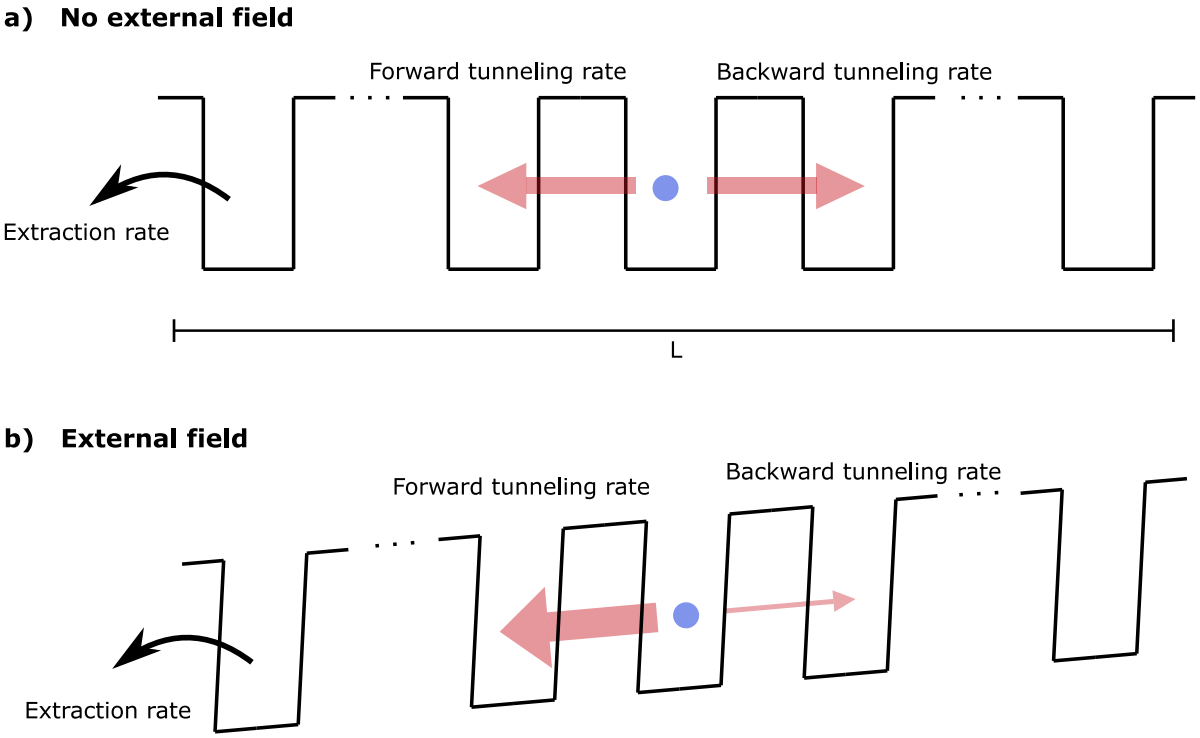

Figure 2.2: Illustration of the interband tunneling process through the miniband in a heterostructure. **a)** No external field is applied and the tunneling rate of a carrier is equal in both directions. **b)** An external field is applied, the probability and consequently the rate of forward tunneling is increased and for backward tunneling is reduced.

2.2 Different mid-infrared detector types

In the following, three state-of-the-art photodetectors in the infrared are presented. Their operation principles are briefly described and their advantages and disadvantages are mentioned.

Mercury cadmium telluride (MCT):

One of the most established infrared detector classes currently available on the market is the MCT (HgCdTe) detector. According to a study in 1959 by Lawson et al. [8], the alloy system composed of $Hg_{1-x}Cd_xTe$ demonstrated semiconducting characteristics over a large portion of the composition range. These materials' energy gap can be altered between 0 and 1.6 eV, depending on their composition. Since then and throughout the

past decades, exploiting this system has been a major focus in research. The advantages of MCT as detector material are clear because until today HgCdTe is the only widely used material that is capable of detecting infrared radiation in both of the atmospheric windows. The mid-wave infrared window (MWIR), which spans from 3 to 5 µm, can be detected with a composition of $Hg_{0.7}Cd_{0.3}Te$ and the long-wave infrared window (LWIR) spanning from 8 to 14 µm with a composition of $Hg_{0.8}Cd_{0.2}Te$ [9]. Regarding detectivity, response speed, power consumption and operation temperature, MCT detectors are superior to many other kinds of detectors. Hence, various MCT detectors are commercially available nowadays, operating at room temperature or cooled in photoconductive and photovoltaic mode. Although it seems that MCT is a perfect material for infrared detectors, it has some fundamental disadvantages and limitations, such as mechanical softness and sensitivity to higher temperatures which can consequently cause tunneling leaking current and dark current. Moreover, long carrier lifetimes and a high dielectric constant result in a frequency response limited to 1 GHz [10, 11]. Also, non-uniformity of the detectivity and the response wavelength are issues related to defects or compositional irregularity [12]. One of the most criticized aspects of the otherwise superbly performing MCT detectors is the inhomogeneity in their growth, as growth stability is especially crucial for the implementation of focal plane arrays (FPA) [13].

Quantum well infrared photodetector (QWIP):

An alternative commonly used infrared detector is the photoconductive QWIP [14]. The detector is based on a GaAs/GaAlAs superlattice structure with an optical transition between a bound electron state in a quantum well and a quasi-bound state close to resonance with the conduction band edge of the employed barrier. By applying an external voltage, the overall energy levels get tilted such that the excited carrier can escape from the well and be collected as photocurrent. The working principle is illustrated in Fig.2.3 a). The detection wavelength spans from 3 to 20 µm and is chosen by designing well width, barrier height, barrier width, well doping density and number of wells [15]. QWIPs have very short carrier lifetimes compared to MCT, on the order of picoseconds [16]. Consequently, they have a very short response time, which is either limited by the carrier lifetimes (for a small number of QWs) or the transit time (for a large number of QWs), whichever is larger. Presently, QWIPs hold the unique position of having high-

speed capability and high absorption for the thermal infrared region, which is beneficial for high-speed applications. Heterodyne detection is even reported up to 110 GHz at 300 K [17]. QWIP focal plane array cameras reached commercial maturity and are used in military, security, surveillance, and medical applications [18]. The main drawback of the otherwise well-performing QWIPs is the considerable dark current which limits the signal-to-noise ratio at higher temperatures and lowers the detectivity. QWIP detectors additionally suffer from a low quantum efficiency.

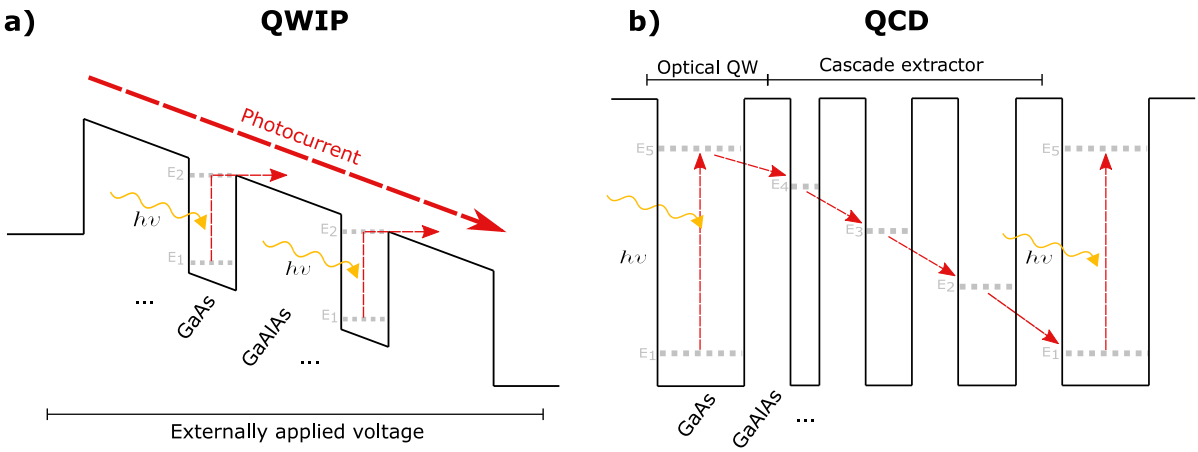

Figure 2.3: Working principle of a QWIP and QCD. **a)** Through photon absorption, the electrons reach the quasi-bound state E_2. By applying an external voltage, the excited carriers get pulled away and contribute to the photocurrent (red arrows). **b)** An excited electron is generated by the absorption of a photon. The cascade excites electron relaxation by longitudinal-optical phonon processes from level E_5 to E_1. Due to the asymmetry of the cascade, the relaxation is mostly in one direction (red arrows), resulting in a net photocurrent.

Quantum cascade detector (QCD):

Another widely used type of detector, which relies on intersubband transitions for light detection is the QCD. It was first reported in 2002 by Hofstetter et al. [19] and further described in 2004 by Gendron et al.[20]. QCDs consist of a succession of coupled quantum wells, for example, out of InAs/AlAsSb or GaAs/AlGaAs. With the absorption of a photon in the quantum well, an electron gets transferred from the ground energy level to a higher energy level. The excited electron gets transferred through a cascade of quantum wells by longitudinal-optical phonon scattering and resonant tunneling until it reaches the ground level in the next optical quantum well, as illustrated in Fig.2.3

b). The quantum wells in the cascade extractor have increasing thicknesses, so that an asymmetric potential is formed and unilateral carrier transport is achieved. By increasing the number of cascade stages, a significant photocurrent is generated without applying any bias, resulting in no dark current noise. The intersubband selection rule in the conduction band dictates that only the electric field component perpendicular to the quantum well layers interacts with optical intersubband transitions. Hence, a suitable light coupling mechanism is required for QCDs, for example, a 45° facet can be used in a double-pass geometry [21]. Since the transport between the subbands typically occurs on the sub-picosecond timescale, electrical detection bandwidths up to several tens of gigahertz at room temperature are enabled [21, 22]. QCDs and QWIPs have a narrow spectral bandwidths due to the intersubband nature of the optical transition, therefore, they need to be acquired or fabricated at the desired emission wavelengths. The interband cascade infrared photodetector (ICIP) does not have this limitation and is recently emerging as a promising candidate for a high-speed and spectrally broadband detector.

Thermal detectors:

Thermal detectors are a class of mid-infrared detectors which are not affected by light-induced transitions of electrical carriers as the just described photodetectors, but are instead based on measuring temperature rises which result from the absorption of photons. The advantage of thermal detectors over photodetectors is that they can be sensitive in very wide spectral regions, and exhibit a nearly constant responsivity over wide wavelength regions. However, they exhibit low speed, moderate sensitivity and low dynamic range which makes them unsuitable for high-speed applications [23].

The bolometer, which was invented in 1878 by S. P. Langley [24], is one of the most widely used thermal detectors. Its operation principle is based on measuring the temperature-dependent electrical resistance. Other examples for thermal detector are the thermocouples and thermopiles [25], and the pyroelectric detectors [26].

2.3 Interband cascade infrared photodetectors (ICIP)

Deriving from interband cascade lasers (ICLs) [27], ICIPs with a type-II superlattice (T2SL) absorbers are a relatively new type of detector, first demonstrated in 2010 by Yang et al. [28]. The operating principle of ICIPs is closely related to that of ICLs,

with the advantage of light detection under normal light incidence, either through the substrate side or via top illumination. Therefore, unlike QCDs, no additional mechanism is required for the light detection due to the interband nature of the optical transition, which is very convenient for various practical applications.

Operation principles of ICIPs:

The integral building blocks of this type of detector are similar to the ones of an ICL. One block is composed on one hand of an electron barrier, which prevents electrons from moving in one direction. This barrier is made of digitally graded GaSb/AlSb quantum wells. On the other hand, a hole barrier consisting of InAs/AlSb quantum wells prevents holes from moving in the opposite direction. In the hole barrier, the exited electrons in the conduction band perform ultra-fast longitudinal-optical (LO) phonon assisted intersubband relaxation and subsequently tunnel into the valence band. The final block is the absorber, which is a type II superlattice with a broken-gap alignment (section 2.1) made of GaSb/AlSb/GaSb/InAs quantum wells, here electron-hole pairs are generated by photon absorption (section 2.1) [29, 7]. The optical transition occurs between the ground state conduction and heavy hole miniband, as displayed in the bandstructure simulations in Fig3.2 and Fig.3.3. The carriers diffuse through the absorber in opposite directions and are blocked in the other direction through the barriers. The two types of carriers eventually recombine at the interface between the electron and hole barriers of adjacent stages or are extracted at the bottom or top contact of the device, as illustrated schematically in Fig.2.4.

In this detector scheme, the same number of photons are needed as the number of stages (cascades) to extract one single electron-hole pair at the contacts. For example, for a three-staged ICIP, three photons are absorbed, generating three electron-hole pairs. Two electron-hole pairs recombine between the adjacent stages and one pair can be extracted at the top and the bottom contact, respectively. The individual absorbers in each section are usually shorter than the diffusion length, resulting in efficient carrier transport and extraction through intraband tunneling (section 2.1). The diffusion length in type II InAs/GaSb superlattice absorber was experimentally determined to be between 0.6 µm and 1.0 µm for temperatures between 250 K and 300 K [13]. Moreover,

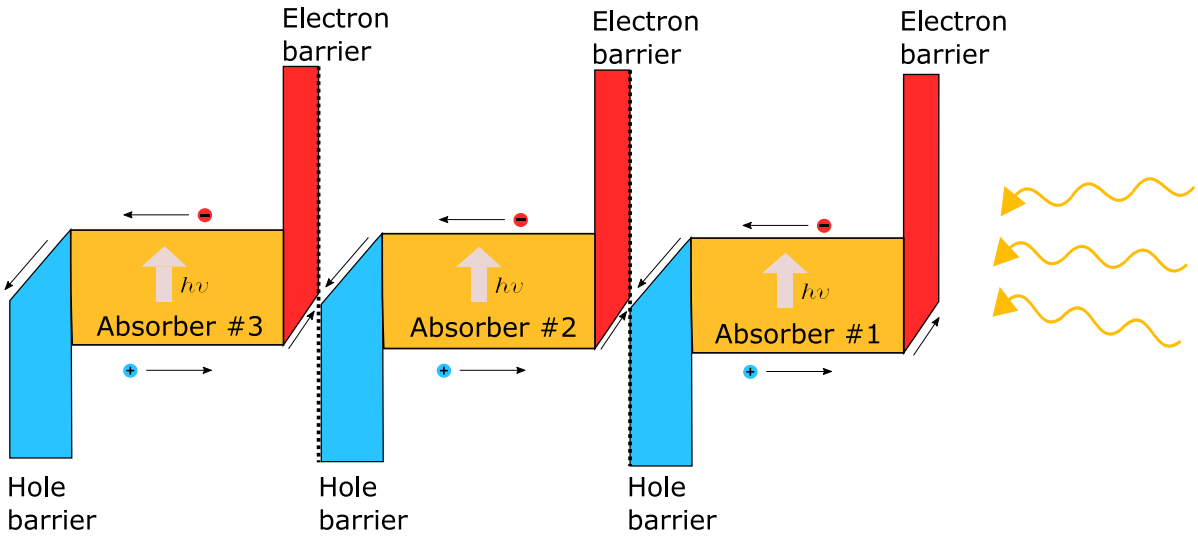

Figure 2.4: Illustration of the operating principle of a three staged ICIP with regular illumination configuration. Each stage is composed of a superlattice absorber, in which an impinging photon gets absorbed and generates an electron-hole pair. Additionally the electron and hole barrier ensure unilateral carrier transport. The generated carriers recombine at the interface of two adjacent cascades or can be extracted at the bottom or top contacts. In order to extract one electron-hole pair at the contacts the same amount of photon need to be absorbed as the number of employed stages.

the thermal and shot noises are suppressed because the noise is proportional to the absorber thickness and inversely proportional to the square root of the number of cascade stages, N_C [13].

Recently, analytical research has been done to determine the maximum detectivity possible in multi-stage ICIPs [30], therefore the performance of a 1-stage, 2-stage, 11-stage and 30-stage ICIP was compared. The analysis shows that the detectivity of a multiple-stage device is approximately 11 % greater compared to an optimized single-absorber detector.

	Advantages	Disadvantage
MCT	• high sensitivity • wide spectral range (1-30 μm) • well established	• growth instabilities • cooling often required • 3-dB bandwidth: 1 GHz [11]
QWIP	• very short carrier lifetimes • high responsivity • wide spectral range (3-20 μm) • 3-dB bandwidth: 110 GHz at RT [17]	• considerable dark current at elevated T • lower detectivity at elevated T • narrow spectral bandwidth (at desired wavelength)
QCD	• low dark current noise • short carrier lifetimes • wide spectral range (1.5 μm-THz range) • 3-bB bandwidth: 21 GHz at RT [21]	• light coupling mechanism • narrow spectral bandwidth (at desired wavelength) • low responsivity
ICIP	• high growth uniformity • wide spectral range (1.8-16 μm) • broad spectral bandwidth (1.8-5μm) (in this work) • 3-dB bandwidth: 7 GHz at RT [31] • suppressed thermal and shot noise proportional to N_c [13] • 3-dB bandwidth of Ga-free ICIPs: 12 GHz at RT [32]	• a relatively new class of detector • carrier dynamics and transport still unexplored • understanding of performance in early stage

Table 2.2: Description of the advantages and disadvantages of the four described mid-infrared photodetectors. The main focus of this comparison lies in their high-speed performance.

A technique to optimize an ICIP's responsivity is current-matching [33]. Light intensity decreases exponentially along the length of the absorber stages due to absorption. The last absorber will therefore be passed by light with the lowest intensity. If all absorbers feature the same length, the last absorber will generate less carriers compared to the first ones. Thus, if the amount of carriers in each stage in not equal, the absorber with the least generated carriers limits the current since an ICIP essentially is an in-series arrangement of cascades. To compensate the attenuated light intensity, the optically deeper absorbers are designed to feature more quantum wells and hence, to be longer compared to the first ones. Consequently, the same amount of carriers is generated in every stage. Depending on the direction of the current flow with respect to the direction of the incoming light, devices are distinguished into two classes [3]. The regular-illumination configuration is encountered if the light first impinges on the electron barrier, as seen in Fig. 2.4, in opposition, if the light first impinges on the

hole barrier reverse-illumination configuration is encountered [13]. The two illumination configurations can be realized by reversing the growth order of layers without changing the direction of the light illumination.
A general overview of the advantages and disadvantages of the four presented mid-infrared photodetectors is presented in Table 2.2. ICIPs show the potential to outperform the currently available state-of-the-art mid-infrared photodetectors.

2.4 Limitation for high-speed performance

In literature, ICIPs are praised as high-speed detectors with a wide spectral bandwidth [29, 31]. By modifying the layer thicknesses of the type-II superlattice absorber, the minibands in the absorber get shifted and the cutoff wavelength of the detector can be tuned. Hence, ICIPs can cover a large range of the infrared spectrum. Various different models of ICIPs, which can operate in the range from 2.9 µm up to 16 µm have been demonstrated so far [1, 13, 34, 35]. Furthermore, room temperature operation has been demonstrated up to a cutoff wavelength of 10.7 µm, where the detectivity of these devices has the potential to outperform commercially available uncooled MCT detectors [34].
Great attention has also been given to the frequency bandwidth of ICIPs. A 3-dB bandwidth of more than 7 GHz at an optical cutoff wavelength of 5 µm was reported recently [31]. Moreover, this year a non-cascaded device featuring an InAs/InAsSb superlattice reached a 3-dB cutoff at 12.8 GHz [32]. Consequently, a lot of research is nowadays made to permanently elevate the 3-dB cutoff frequency of the devices.

Transport limitations:
For conventional absorbers in which the diffusion of the carriers is the main transport process, the cutoff frequency is given by Eq.2.9 [36].

$$f_{3-dB} = \frac{2.34D}{2\pi t^2} \tag{2.9}$$

D and t are the diffusion coefficient and the absorber thickness, respectively. The frequency bandwidth simply increases by reducing the absorber thickness. However, the device's sensitivity and the signal to noise ratio (SNR) decreases as well since less carriers are generated through the absorber. By the multi-stage architecture of the ICIP, this

drawback can be avoided. The individual thickness of the absorber in each stage can be designed to be short so than the carrier transit time across every stage is reduced to the picosecond timescale. Additionally, by serially stacking multiple cascade stages, enough photons are absorbed to ensure high sensitivity and suppress noise. It has analytically been shown how multi-stage ICIPs can be advantageous over the conventional single-stage detector [30]. Also, the specific detectivity D* increases since it is proportional to the square root of the number of stages Nc in a first order approximation, $D^* \propto \sqrt{N_c}$ [7]. Additionally, by current matching of the stages, the responsivity gets maximized furthermore. Hence, ICIPs can respond quickly to direct optical modulation at high frequencies at room temperature and above.

Parasitic effects:

The electrical limitations also need to be considered when integrating an ICIP into a circuit. In order to exploit the high-speed detection capabilities of an ICIP, all parasitic components must be minimized. The equivalent circuit of an ICIP device is composed of a current source in parallel to the parasitic device resistance R_D and the parasitic device capacitance C_D, as illustrated in Fig.2.5. L is the parasitic inductance caused by the wire bonds and Z_L is the 50 Ω load resistance.

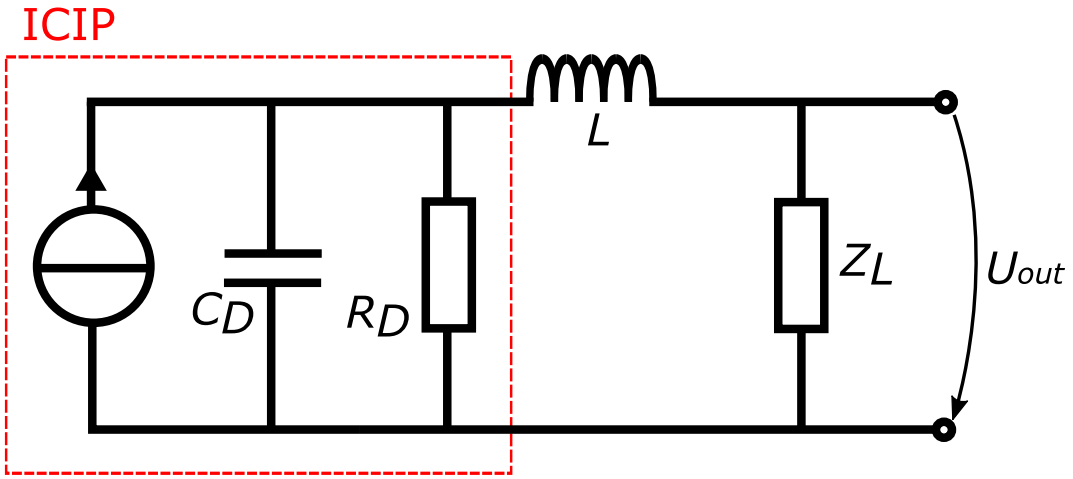

Figure 2.5: Equivalent circuit of the ICIP. R_D and C_D are the parasitic resistance and capacitance of the detector. L is the parasitic inductance originated by the wire bonds. Z_L is the 50 Ω load resistance.

The electrical power frequency response $R(\omega)$ of this system is given by Eq. 2.10 [21].

$$R(\omega) = \left| \frac{U_{out}(\omega)}{U_{out}(\omega = 0)} \right|^2 = \frac{1}{(1 + \frac{Z_L}{R_D} - \omega^2 L C_D)^2 + \omega^2 (\frac{L}{R_D} + Z_L C_D)^2} \tag{2.10}$$

This circuit behaves like a low-pass filter, whose 3-dB bandwidth depends strongly on the parasitic inductance and capacitance, thus both need to be minimized. Especially the high-speed performance suffers from the introduced LC resonance since the frequency response decreases by $1/\omega^4$ (40dB/decade) above the cutoff frequency. The parasitic inductance can be traced back to the gold wire bonds, which are used to connect the detector with the circuit. Those can be shorted by directly attache the device to the coplanar waveguide, thus a shorter distance needs to be covered for the bonding. The parasitic capacitance of the device can be approximated by the formula for a parallel-plate capacitor Eq. 2.11.

$$C = \epsilon_0 \epsilon_r \frac{A}{d} \qquad\qquad f_{RC,cutoff} = \frac{1}{2\pi RC} \tag{2.11}$$

Consequently, the capacitance can be minimized either by reducing the area A or by increasing the distance d between top and bottom contact, ϵ_0 and ϵ_r denote the vacuum and relative permittivity, respectively. The parasitic capacitance could be reduced by utilizing more cascades and so increasing the distance d. An alternative option is to increase the single absorber thickness t with the consequence of reaching the transport limitations, as mentioned in the previous section. The area can also be reduced to increase the cut-off frequency. One common drawback of a smaller area is however the reduction of the DC signal. This occurs because the beam spot of the impinging light is normally larger than the detector area and consequently for smaller areas less photons get absorbed compared to a detector with a larger area.

Finally, to reach high-speed performance with the ICIPs the transport and electrical parasitic limitations need to be considered and a trade-off between absorber size and thickness, cascade stages, and generated electrical signal needs to be found.

3 Sample Fabrication

In the following chapter, the realization of the devices is shown. First, the MBE growth of the structure, the band simulation of different absorber thicknesses and the design of the ICIP is described. Finally, the cleanroom fabrication and mounting of the devices is presented.

3.1 MBE growth and structure design

All realized ICIP structures were grown by *Nanoplus GmbH* [37] through molecular beam epitaxy (MBE) on a compensation-doped GaSb substrate for the PhD work of H.Knötig [3]. Additionally, a 500 nm thick GaSb bottom contact was grown with a doping of $n = 1$ x 10^{18} cm^{-3}. In order to balance the strain in the structure, a 60 nm thick transition layer was inserted between the bottom contact layer and the first electron barrier. For the active region, an electron barrier with a thickness of 27 nm was grown, followed by the absorber, which consists of a GaSb/AlSb/GaSb/InAs type-II superlattice. This design was previously reported by Lei et al. [13]. A 69 nm thick hole barrier was grown and then the active region was extended into a total of three cascades of electron barrier, absorber and hole barrier. Finally, the top contact was realized as a highly doped $n =$ 2 x 10^{18} cm^{-3} layer with a thickness of 50 nm. A schematic of the grown structure with an absorber length of 351 nm is presented in Fig.3.1.

A regular-illumination configuration is realized, as shown in Fig.2.4, since the devices are illuminated from the substrate side. However, a double-pass geometry is in fact obtained because the top contact is entirely metallized and reflects the propagating light. As a result, the device's current matching to maximize utilization of absorbed photons [33] is (at least in a first estimate) not necessary. The light propagates from the substrate to the top contact of the detector, where it gets reflected at the metallic interface and returns back to the substrate. During this path, the light intensity gets attenuated continuously. This implies that the first absorber stage gets passed by the light with maximum intensity and by the reflected light with the greatest attenuation. Consequently, the amount of photons absorbed in each step should be roughly equal, given the variation in light intensity in the two directions.

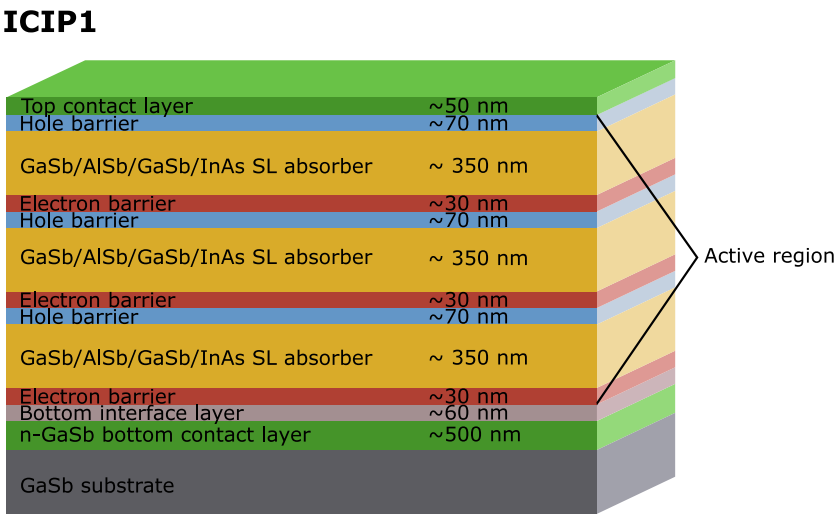

Figure 3.1: Schematic of the grown ICIP structure. The active region consists of three cascades composed of the electron barrier, the absorber and the hole barrier.

In order to investigate the limitation of the high-speed performance in dependence on absorber length of the devices, two different structures are compared. The absorber structures differ in the number of absorber superlattice periods as followed:

ICIP1: 54 x absorption section $\rightarrow$ 351 nm
ICIP2: 18 x absorption section $\rightarrow$ 117 nm

Simulations of the bandstructure of ICIP1 and ICIP2 are made in the scope of the of PhD theses of H. Knötig [3] and are presented in Fig.3.2 and Fig.3.3. The simulations are made at zero bias and they show a potential barrier that carriers need to overcome before being extracted from the superlattice absorber. In Fig.3.2 a) the 351 nm superlattice absorber of ICIP1 is seen compared to the 117 nm superlattice absorber in Fig.3.2 b). The absorber thickness of ICIP2 is around one third of the absorber of ICIP1, which is favorable for high-speed performance since the carriers need to travel a shorter distance until they get extracted. A closeup of the simulation of the electron and hole barrier is seen in Fig.3.3 a) and in Fig.3.3 b) a magnification of the superlattice absorber of ICIP1 is shown.

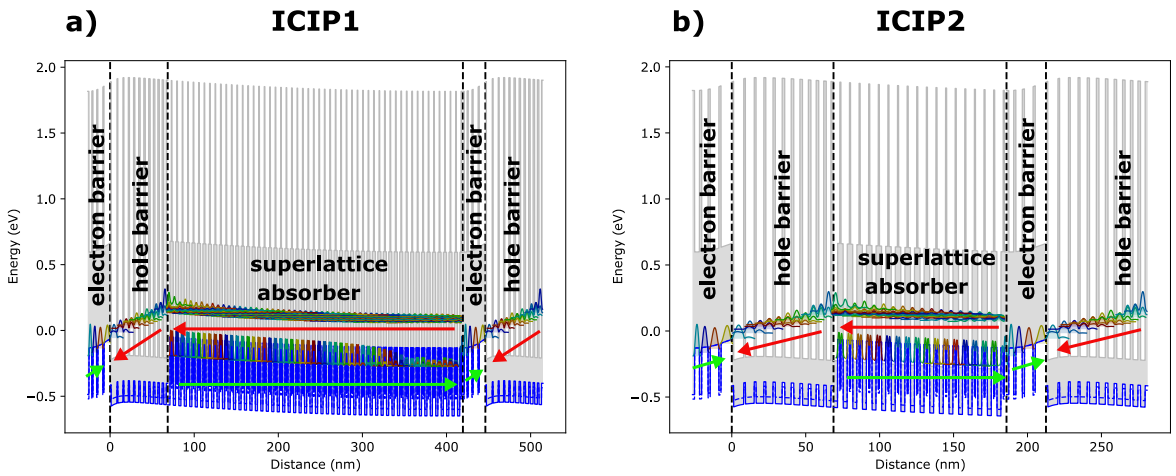

Figure 3.2: **a)** Simulated bandstructure of ICIP1. The directions of the carrier transport are indicated by red and green arrows for electrons and holes, respectively. **b)** Simulated bandstructure of ICIP2 with reduced absorber length. Figures are taken with permission from [3].

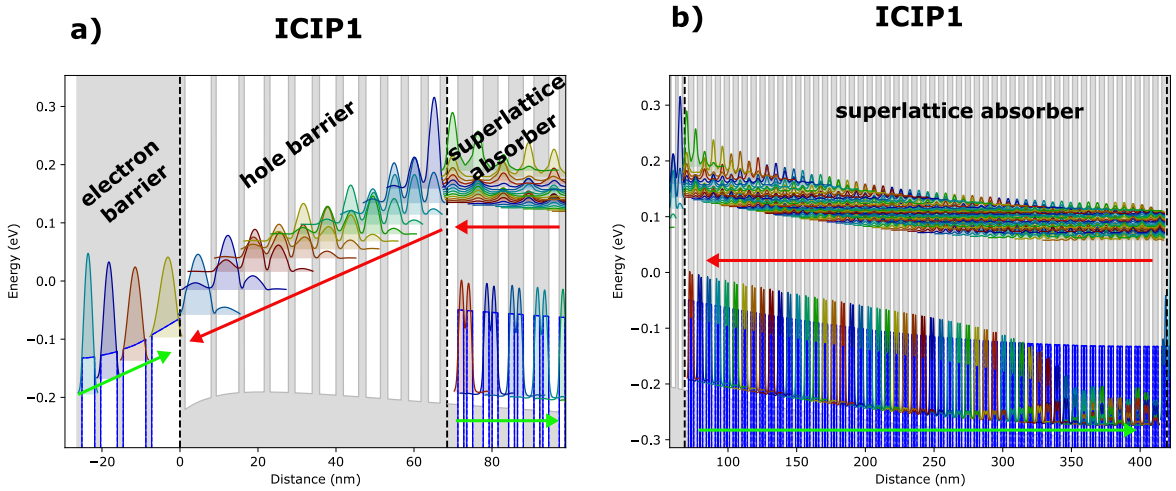

Figure 3.3: **a)** Magnification of electron and hole barrier. After the carriers get extracted from the superlattice, they recombine at the interface between two adjacent cascades. **b)** Zoom of the superlattice absorber, the formation of the miniband in the conduction band is visible. Figures are taken with permission from [3].

3.2 Design of the devices

The size of the devices influences the high-speed performance, thus circular devices with different diameters from 20 µm to 2000 µm were fabricated. As seen in Eq.2.11 a larger area A increases the capacitance C and consequently decreases the 3-dB RC cutoff frequency. The smallest devices with a diameter of 20 µm have therefore the highest cutoff frequency. However, by reducing the diameter of the devices, the absorber area also decreases, which results in a lower electrical signal since fewer photons get absorbed.

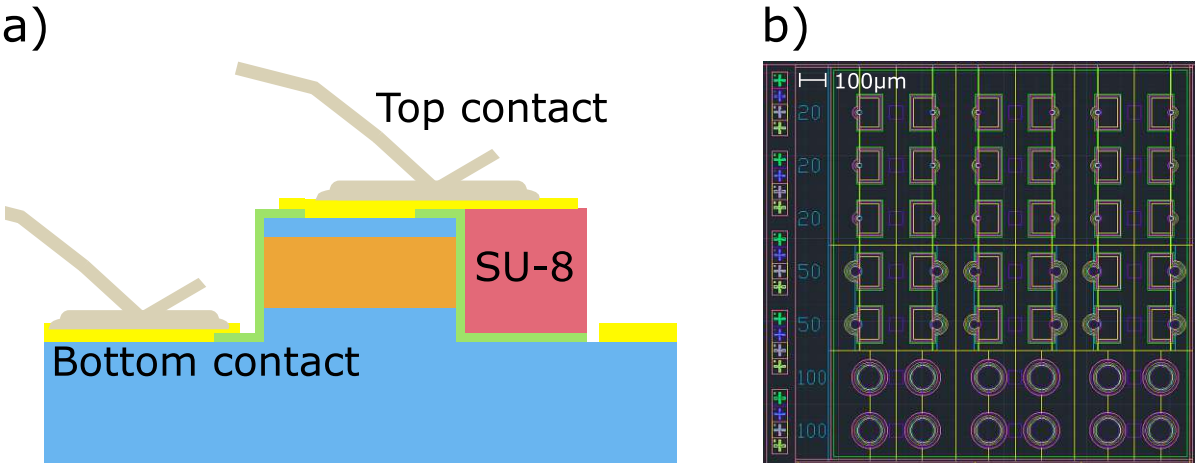

Figure 3.4: **a)** Schematic of a finished device with the extended SU-8 pad. Due to the enhanced area of the top contact, the device can directly be wire bonded. **b)** A section of the designed photomask in *AutoCAD*. The 20 µm and 50 µm diameter devices are designed with an additional contact pad.

The devices fabricated in previous work [3] within this research group were contacted by using a ground-source-ground (GSG) probes. However, since electrically contacting a large number of devices with this method can be a time consuming process, a new design for the ICIPs is developed to directly wire bond the top contacts of even the smallest devices.

A gold wire can be bonded directly onto the metallized surface of a mesa with a diameter larger than 100 µm. This is not possible for the smaller devices since the average dimension of a wedged wire bond with the available *iBond5000-Wedge* machine is 75 µm. To extend the area of the top contact for the 20 µm and 50 µm diameter mesas an additional SU-8 photoresist contact pad is designed, as illustrated in Fig. 3.4 a). The contact pads are located directly next to the mesa and designed in a rectangular shape, as shown in

the *AutoCAD* mask in Fig.3.4 b). They have a width of 80 µm and a length of 120 µm so that the bond can exactly fit onto it. Since the metallized contact pads form a plate capacitor by themselves, the dimensions of the pads have to match the desired cutoff frequency. The dielectric constant of SU-8 is approximately $\epsilon_r = 3$ [38] and with a height of $d = 3\,\mu m$ this results in a capacitance of $C = 85\,fF$. According to Eq. 2.11 and with a $50\,\Omega$ impedance matched circuit, it leads to a cutoff frequency $f_{RC,cutoff} = 37\,GHz$ which is much higher than the expected optical cutoff frequency.
To realize a homogeneous layer of SU-8 for the extended contact pads, a SU-8 standard recipe needed to be developed and then integrated into the ICIP fabrication process.

3.3 SU-8 Photoresist

SU-8 photoresist is an epoxy-based negative photoresist which is commonly used in the fabrication of micro- and nano-structures [39, 40]. When exposing SU-8 to UV (350-400 nm) radiation, the molecular chains cross-link, causing a polymerisation which makes it insoluble to the photoresist developer. By using different viscosities of the photoresist, layers of thicknesses ranging from 0.5 µm up to above 200 µm can be formed through spin coating. SU-8 has excellent imaging characteristics and is capable of producing structures with very high aspect ratio and nearly vertical sidewalls. Cured cross-linked SU-8 is difficult to remove and best suited for permanent applications.
The data sheet of the SU8-2000 photoresist series of *MICROCHEM* describes the film thickness dependenc over the spin speed of SU-8 resists with different viscosity [41]. In order to get a layer thickness of around 3 µm two different options are probed. First, the SU8-2005 photoresist is spin coated at 2000 rpm, second, the SU8-2002 photoresist at 1000 rpm. The viscosity of the SU8-2005 series is noticeably higher than the SU8-2002, which makes it harder to spin-coat the resist onto the surface of the sample. The best results are obtained by spin coating the SU8-2002 photoresist with 2000 rpm, hence, this parameters are used in all the following steps.
A common issue with high viscosity fluids and thick coatings is the formation of edge beads. In the SU-8 spin coating process, the edge beads form depending on various parameters, such as spin speed, surface tension and viscosity. Due to the centrifugal force, the SU-8 flows away from the center of the substrate, resulting in a uniform thickness of SU-8. At the edge of the sample, the surface tension of SU-8 makes it difficult to

detach. Since the SU-8 has a high viscosity, the generated edge bead cannot reflow by gravity force. The edge beads can then cause an air gap between the substrate and the photomask during the UV exposure, which results in non-uniform patterns on the sample. Furthermore, the sample might break since the edge bead is in contact with the mask. In literature, a variety of different treatments for the edge beads have been reported [42, 43, 44].

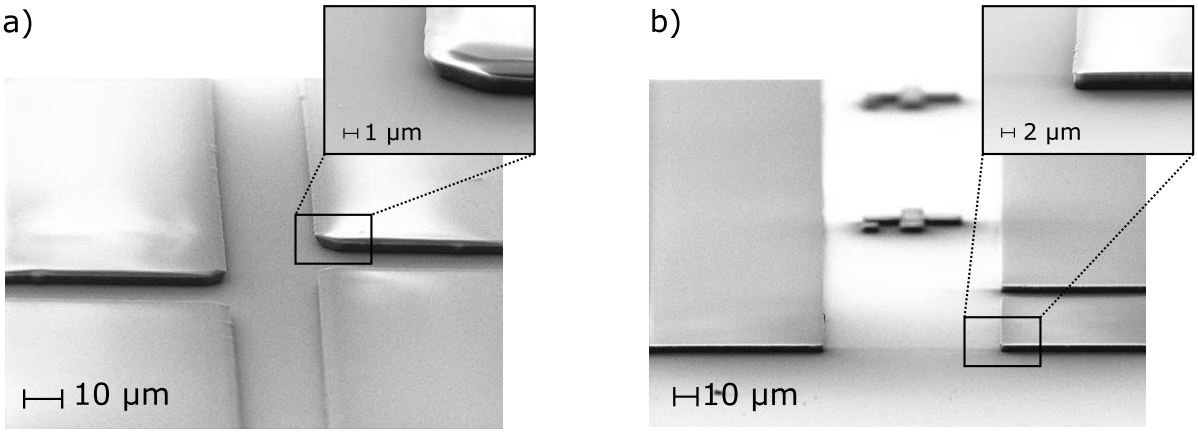

Figure 3.5: SEM images of the optical lithography tests for the SU-8 photoresist. **a)** Over exposure of the resist film results in negative sidewall profiles. **b)** Optimized exposure and development times of the resist lead to near vertical side walls.

One of the most common treatments to remove the edge beads is to spray out edge bead removal (EBR) fluid over the entire surface of the photoresist. The EBR is dissolved into the SU-8 which decreases the viscosity and enables a reflow of the resist to the center. After 24h of slow drying, all the EBR is evaporated. This method is usually used for wafer substrates starting from three inch wafers, but no satisfying results are achieved by applying this technique on smaller sized 1 cm x 1 cm substrates, as needed for this work. Higher edge beads are formed in the corners of the rectangular substrate compared to the sides, which causes an inhomogeneous reflow of the resist. This results in a non-uniform thickness of the SU-8 over the whole substrate. The best approach to remove the edge beads on the rectangular substrates is to physically remove them with a cleanroom-grade cotton swab. This can easily be done in the spin coater, directly after the coating of the SU-8, while the sample is still fixed to the chuck with vacuum suction.

Finally, a recipe for the optical lithography is developed. In order to obtain near vertical sidewalls, some adjustments are made from the recommended exposure and development time of the *MICROCHEM* data sheet [41], as shown in Fig. 3.5.

Standard recipe: For a 3 µm thick layer with SU-8 2002 *MICROCHEM*

1. Spin Cycle: First ramp to 500 rpm at 100 rpm/s acceleration. Finally, ramp to final spin speed of 2000 rpm at an acceleration of 300 rpm/s and hold for a total of 30 seconds.
2. Edge beads removal: Physical removal with a cleanroom swab.
3. Soft Bake: On a hotplate at 65 °C for 1 minute, then ramp to 95 °C with a rate of 30% and finally, hold for 2 minutes.
4. Exposure: UV exposure with mask aligner *Karl Suess MJB4 aligner* for 5 seconds.
5. Post Exposure Bake (PEB): On a hotplate at 95 °C for 2 minutes.
6. Development: Dip in developer *micro resist technoloy mr-Dev 600* for 10 seconds, afterwards rinse with water for 1 minute.
7. Hard Bake (cure): On a hotplate at 150 °C for 30 minutes.

3.4 Fabrication of the ICIPs

In the following, all processing steps for the entire fabrication of the newly designed ICIPs are explained. All fabrication stages are shown in the schematic Fig.3.7 for reference (A-T).
Initially, the MBE grown material is cleaved in 1.1 cm x 1.2 cm pieces for further processing steps. In the scope of this work, one piece of each absorber structure is fabricated into devices. After an acetone and isopropyl alcohol cleaning step (A), a 500 nm thick layer of Si_3N_4 as hardmask is deposited onto the top side of the material (B) using plasma enhanced chemical vapor deposition (PECVD). The hardmask is first structured by optical contact photolithography (C) and then etched using a CHF_3/O_2-chemistry process by reactive ion etching (RIE) (D). The photoresist is then removed by acetone and isopropyl alcohol, furthermore, to remove all residuals the samples are put into an

oxygen plasma (E). The mesas are subsequently etched using a Cl/Ar-chemistry process with RIE (F). It is crucial at this etching step to reach the n-doped GaSb layer, which is designed as the bottom contact layer for the devices. Since ICIP1 and ICIP2 have different absorber length the etching depth is 1780 nm and 880 nm, respectively. Afterwards, the hardmask is fully removed with SF_6-chemistry by RIE (G). Next, a 250 nm thick layer of Si_3N_4 is deposit by PECVD (H) for the electrical passivation. The dielectric layer is then defined by the optical lithography and etched by RIE so that the passivation layer still covers the sidewalls with a 5 µm overlap on the top and bottom of the mesa structures (I-K).

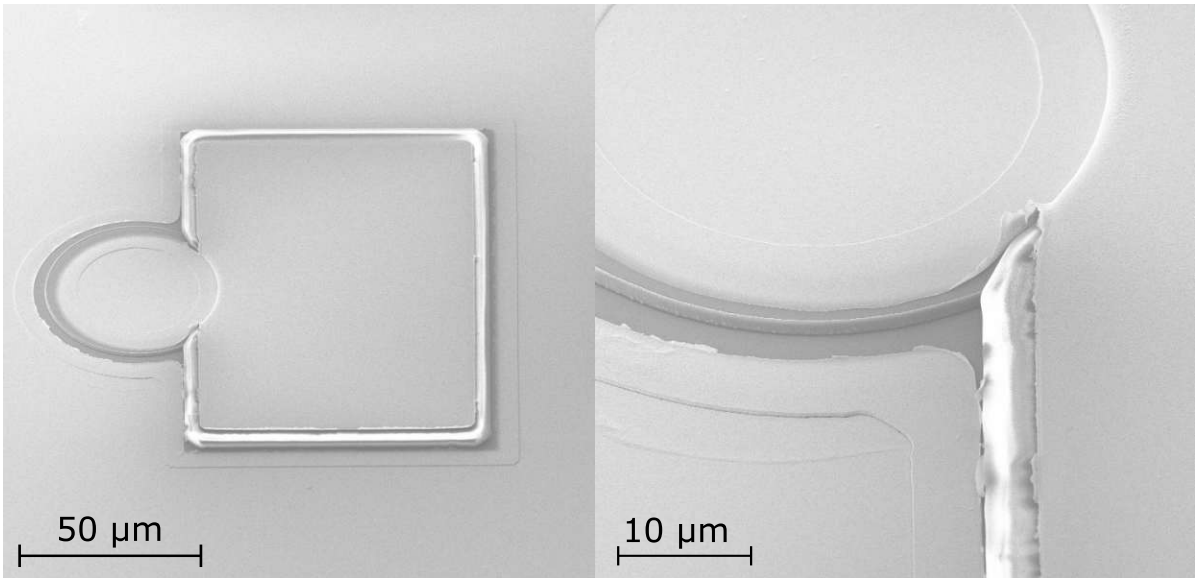

Figure 3.6: SEM micrograph of the sputtered contacts of the ICIP structures. The surroundings of the structure are covered by the bottom contact as seen on the left side. On the right side a closeup of the extended top contact is seen. The top contact covers the SU-8 pad and the surface of the mesa.

The ohmic bottom contacts are fabricated using a lift-off process. Therefore, a 250 nm thick metallization layer composed of Ge/Au/Ni/Au is sputtered onto the surface of the samples (L-M). The lift-off is then completed using acetone in an ultrasonic bath (N). After the lift-off, the samples are thermally annealed at 310 °C for 60 seconds using rapid thermal annealing (RTA). Subsequently, a 3.5 µm thick layer of SU-8 photoresist is deposited by spin coating as described in the previous section 3.3.

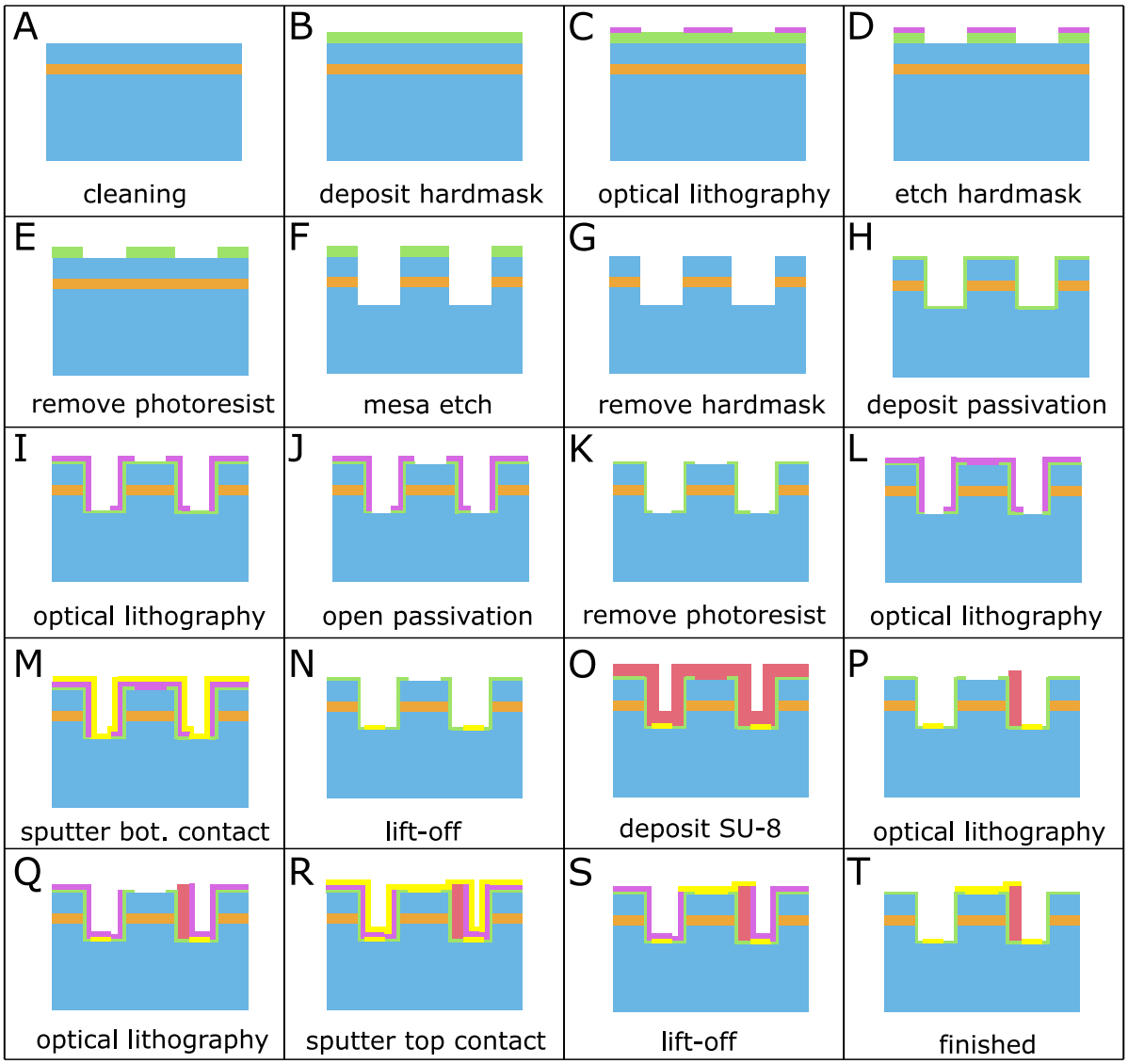

Figure 3.7: Schematic of the individual processing steps necessary for the fabrication of the ICIPs. The cross section of one ICIP mesa structure is illustrated with the absorber region represented with an orange colour. The Si_3N_4 layers are pictured in green and the photoresist is painted in violet. The SU-8 photoresist is illustrated with salmon colour and the metallization is represented in yellow colour. **A, E, K, N, S:** acetone and isopropyl alcohol; **B, H:** PECVD; **C, I, L, P, Q:** mask aligner; **D, F, G, J:** RIE; **M, R:** sputter system; **O:** spin coater.

The desired contact pad geometry is then defined by the optical contact photolithography and cured on a hotplate at 150 °C for 30 minutes (O-P). For the metallization of the enhanced top contacts a 250 nm thick layer of Ti/Au is sputtered onto the complete surface, which is then structured by a lift-off process using an acetone and isopropyl alcohol bath (Q-S). A scanning electron microscope (SEM) micrograph of the extended top contacts is shown in Fig.3.6. Finally, the samples are cleaved into smaller pieces and cleaned again to remove the impurities from cleaving.

3.5 Mounting

The fabricated samples ICIP1 and ICIP2 are cleaved into smaller pieces. The sections with the 20 µm, 50 µm and 100 µm diameters mesas are cleaved into pieces of 1.5 mm x 3.5 mm as seen in the blue rectangle in Fig.3.8 a). Half of the cleaved sample is just covered with gold and has no structure on it. This part was designed as an extra space for attaching the sample to the 50 Ω coplanar waveguides, which are optimized for radio frequency extraction and can be attached to a 2.92 mm end-launch connector, as illustrated in Fig.3.8 b).

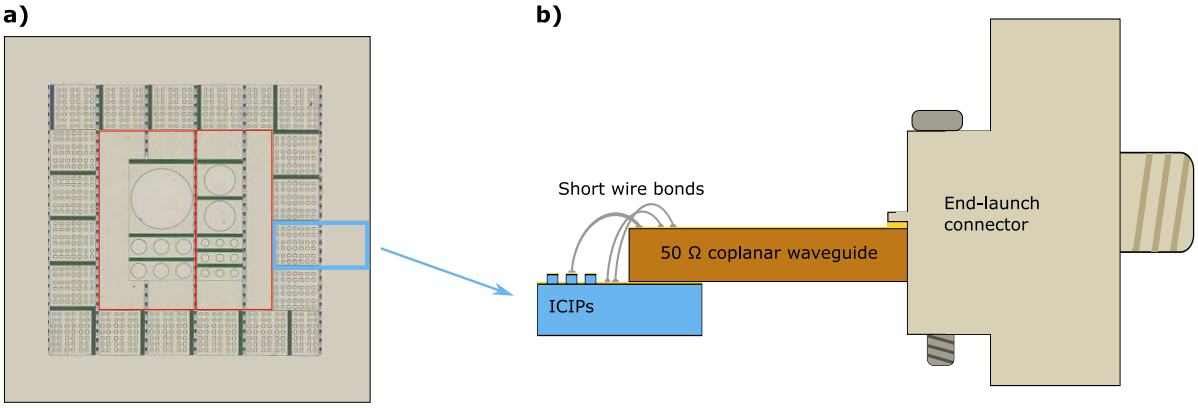

Figure 3.8: a) Finished ICIP1 sample with the 20 µm to 2000 µm diameters devices. The blue rectangle represents the size of the cleaved samples which are used for the high speed application. The red rectangles represent cleaved sections for the bigger sized mesas. Those are used for the characterization of the devices. **b)** Schematic of the mounted and wire bonded device, which is connected trough the coplanar waveguide to the end-launch connector.

The sections with the bigger sized mesas are cleaved into two larger parts, as shown in the red rectangle in Fig.3.8 a). These devices are not used for high-speed applications. Therefore, they are mounted on a copper plate which has a rectangle cutout so that the substrate below the realized devices is still visible for the impinging light. Finally, these mesas are electrically bonded by longer wire bonds to a printed circuit board (PCB). In order to attached the devices to the coplanar waveguide or the copper plate a two-component adhesive was used and afterwards let dry for 30 minutes.

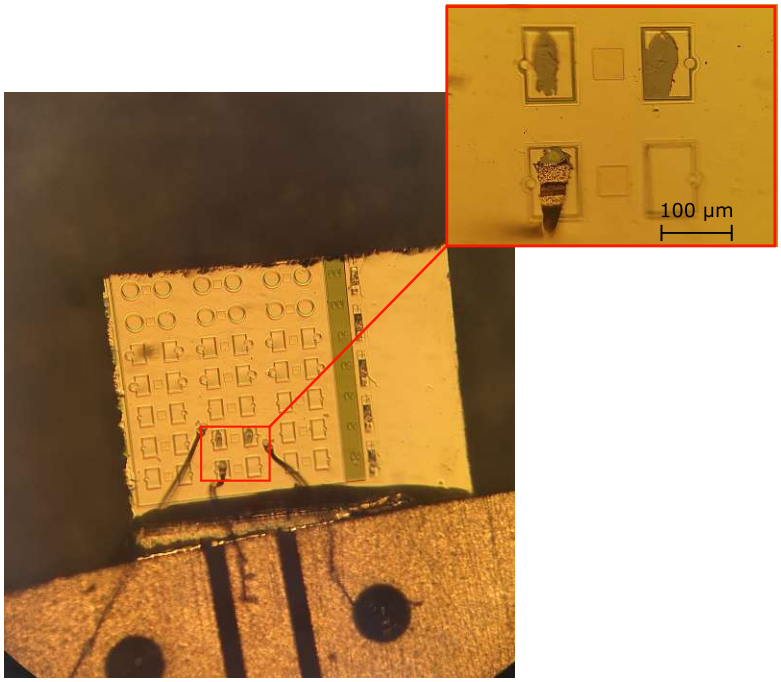

Figure 3.9: Microscope picture of a mounted and wire bonded device. The bottom contact extends all the surrounding of the mesas and contact pads and is designed to reduce the series resistance by upsizing the area. On top of the magnification two contact pads are seen where the wires ripped off. At the bottom, a successfully bonded wire is presented.

To electrically contact the smaller devices, which are design for high-speed performance, first, two short gold wires are bonded from the ground contact of the coplanar waveguide to the bottom contact of the devices. One short bond wire is then used to connect the signal stripe of the coplanar waveguide with the top contact of the device. Unfortunately, the wire bonds on the extended SU-8 contact pad rip-off easily, as dis-

played in Fig.3.9. The detached bond wires also stripped the gold metallization of the pad, thus, no rebonding on this device is possible. By adjusting the bonding parameters it was possible to tackle this problem, however, the bonds were still susceptible to breakage due to vibrations. Finally, the coplanar waveguide with the mounted and bonded device was fixed into the end-launch connector and measured, which is described in the following chapter, in Fig. 3.10 the fully mounted device is presented.

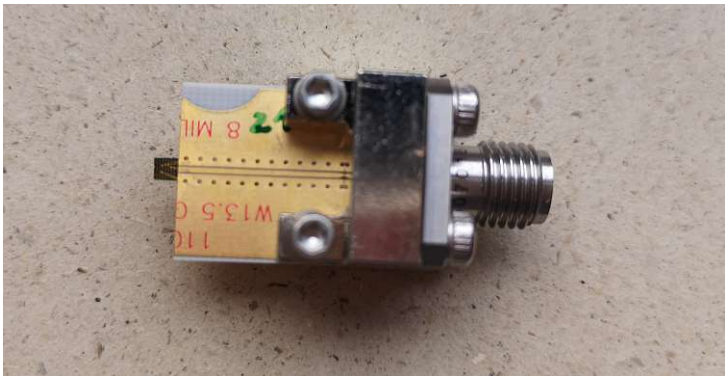

Figure 3.10: Picture of the fully mounted ICIP. The device is attached to the coplanar waveguide with a two-component adhesive and connected through short bond wires. The coplanar waveguide is finally fixed into the 2.92 mm end-launch connector.

4 Measurement Results

In this chapter, first the electrical and then the optical characterization of the devices is described. At the end, two high-speed applications are presented in which the detectors were employed. The devices used in the measurements are labeled ICIP11 and ICIP12 for the absorber design 1 (351 nm) and ICIP21 and ICIP22 for design 2 (117 nm).

4.1 Electrical Measurements

This section describes the electrical characterization of both ICIP designs by an electrical rectification and a current-voltage measurement.

Electrical rectification:
The electrical rectification of the ICIP devices was measured with an electrically modulated signal. The complete measurement setup is illustrate in Fig. 4.1.

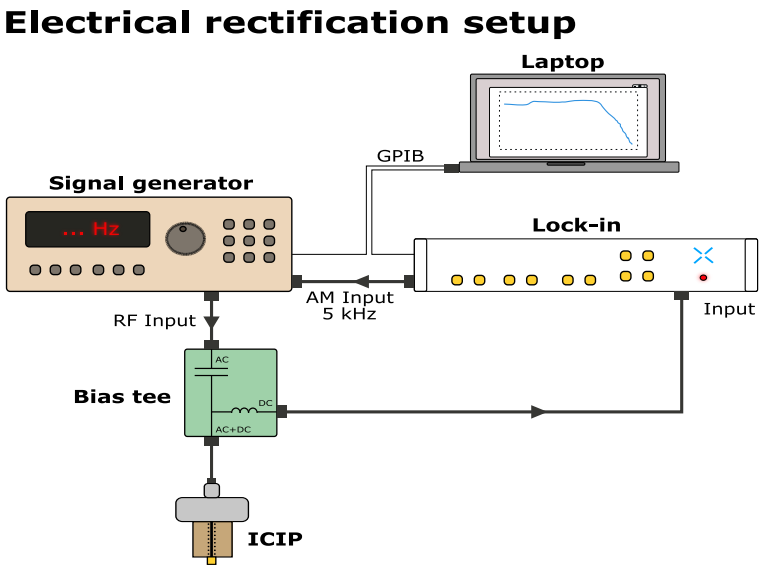

Figure 4.1: Illustrated setup of the electrical rectification measurements. The ICIP device is directly connected through a bias tee to a signal generator and a lock-in amplifier.

A signal generator was amplitude-modulated (AM) with a 5 kHz sine waveform provided by a lock-in amplifier. The carrier frequency was then swept from 10 MHz to 20 GHz

and fed into the ICIPs via the AC port of a bias tee with a lower cutoff frequency of 20 kHz. The nonlinear behavior of the ICIP demodulates the signal down to 5 kHz where it is subsequently measured by the lock-in amplifier over the DC port of the bias tee.

The results of the measurements are presented in Fig. 4.2. The rectified power shows a lowpass response which can be ascribed to the parasitic components of the device and of the setup. The device resistance was between 0.6 - 8 kΩ, depending on the size of the mesa. Due to the 50 Ω impedance of the transmission line the device resistance can be neglected when examining the equivalent circuit behavior (seciton 2.4). Consequently, the lowpass characteristics should mainly originate from the parasitic capacitance of the device and the parasitic inductance of the bond wires. The obtained data does not correspond to the expected results, since the 3-dB cutoff was expected to be much higher. For ICIP11, ICIP12, and ICIP22 the 3-dB cutoff frequency is in the lower MHz range at 0 V bias, which is way below to the estimated electrical cutoff frequency obtained form Eq. 2.11. This suggests that the diffusion-limited transport is visible in the electrical rectification measurements.

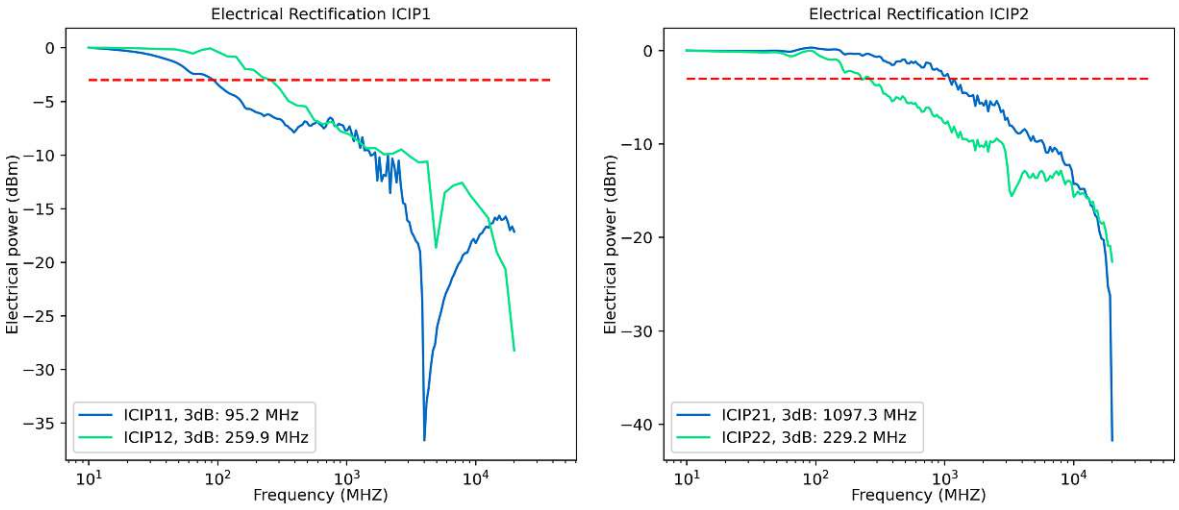

Figure 4.2: Electrical rectification measurements for the 20 µm devices. On the left side the results of two ICIP1 devices and on the right side of two ICIP2 devices are presented. The red dashed horizontal line marks the 3-dB power cutoff.

Current density - voltage characteristics:

In the following, the dark current density versus the bias voltage was investigated. Therefore, two devices per ICIP design with diameters of 20 µm were measured at room temperature, the results are presented in Fig.4.3. The the dark current values are relatively high compared to values reported in the literature [29, 31]. The high dark current density can be explained by the fact that the current density-voltage characteristic is sensitive to the size of the devices [13]. It has been shown that the leakage current scales linearly with the circumference of the mesas [3]. Therefore, reducing the dark current is especially important for detectors with smaller diameters. Additionally, different passivation techniques have been reported in literature [45, 46] to reduce the sidewall leaking, as for example with SU-8 photoresist or aqueous ammonium sulfide solutions.

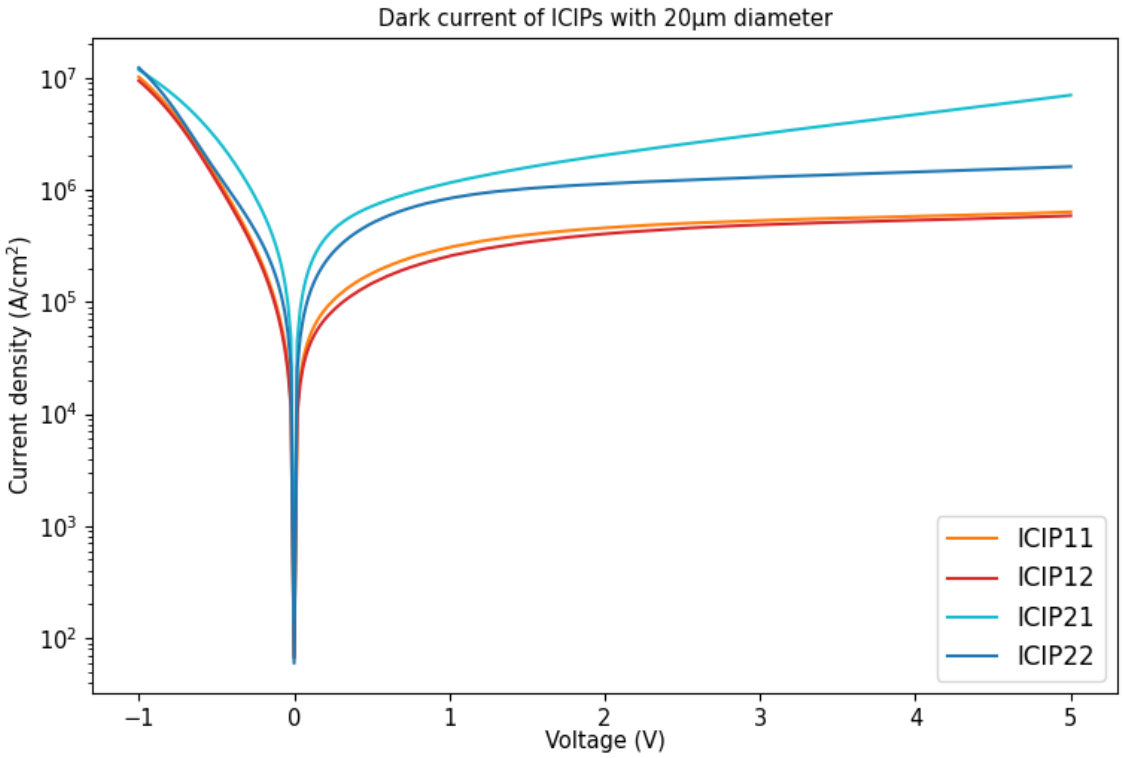

Figure 4.3: Dark current density versus the bias voltage for two ICIP1 and two ICIP2 devices with a diameter of 20 µm. Measurements were taken at room temperature.

4.2 Optical Measurements

In the following section, the optical performance of the realized ICIP1 and ICIP2 devices is investigated. Therefore, their responsivity is characterized and additionally, the radio frequency (RF) response is analyzed using a direct modulation setup first and finally an optical parametric oscillator (OPO) setup.

Responsivity:

The responsivity is defined as the electrical output signal of the detector in response to a given incident radiant power. Thus, it can be obtained using Eq. 4.1 where η is the quantum efficiency, q the elementary charge and $h\nu$ is the energy of the incident photons. Consequently, the unit of the responsivity is given in amperes per watts (A/W).

$$R = \frac{\eta q}{h\nu} \qquad \Rightarrow \qquad R = \frac{I}{P} \tag{4.1}$$

As mentioned in the previous chapter, ICIPs with diameters up to 2 mm have been fabricated to facilitate the characterization of the devices. The realized 1 mm diameters devices of the ICIP1 and ICIP2 designs have been used for the responsivity measurements. Since the high-speed performance is irrelevant for this measurement, the devices have been mounted on a copper plate and were connected to a simple printed circuit board (PCB). The large sized mesas ensure that all incident light can be focused onto the detector, making the measurements of the responsivity a lot easier.
The spectral response of the mid-infrared globar source from the Fourier-transform infrared spectrometer (FTIR) was recorded with a thermal detector first, since the intensity of the globar is not constant over the spectrum. Hence, to guarantee a correct response measurement of the ICIPs, the wavelength dependent output power of the globar needs to be considered. Finally, the spectral response of the two ICIPs was measured with the FTIR over a broad spectrum. The absolute values of the responsivity were determined by using an ICL as a reference. The emitted output power of a 3.3 µm singlemode ICL was first measured with a power meter. Next, the entire radiation of the laser was focused onto the detector and the generated photocurrent was measured. Consequently, by applying the right equation of Eq.4.1 the absolute responsivity of the detector at 3.3 µm can be calculated. The spectrally-depent responsivity can subsequently be obtained from the globar measurement according to this reference value. The measured responsivity for

the ICIP1 and ICIP2 design are shown in Fig.4.4 and Fig.4.5, respectively. The results of the responsivity measurement of ICIP1 are comparable to the values from Lei et al. [13], where the design of the absorbers was adapted from. Surprisingly, the responsivity of ICIP2 is just slightly lower than the one of ICIP1. This was not expected since the absorber length of ICIP2 is reduced by one third compared to ICIP1. Hence, also the responsivity of ICIP2 was expected to be reduced by one third. The spectral bandwidths of the two different designs are very similar, ranging from 1.8 µm to 5 µm. By modifying the superlattice structure, the cutoff wavelength can even be increased. Furthermore, the measurements were taken under ambient conditions, and two CO_2 absorption bands, which lie within this range, can be seen in the plots. The broad spectral response is very convenient for the characterization of lasers and frequency combs, which emit at various wavelengths, and for many other applications in the mid-infrared.

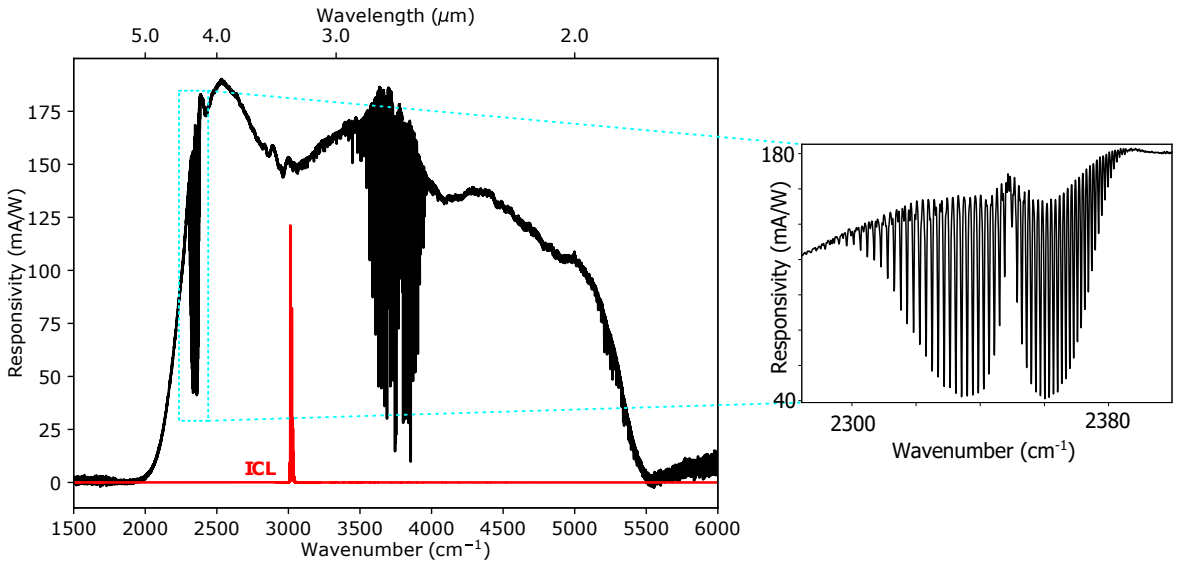

Figure 4.4: The measured responsivity of the 1 mm sized mesa of ICIP1 is plotted in black. Additionally the spectrum of the ICL, which was used for the characterization is plotted in red. Since the measurements were performed under ambient condition two CO_2 absorption bands can be seen in the spectrum. A magnification of the absorption lines between 4 µm and 5 µm is shown on the right side. Figure taken with permission from [3].

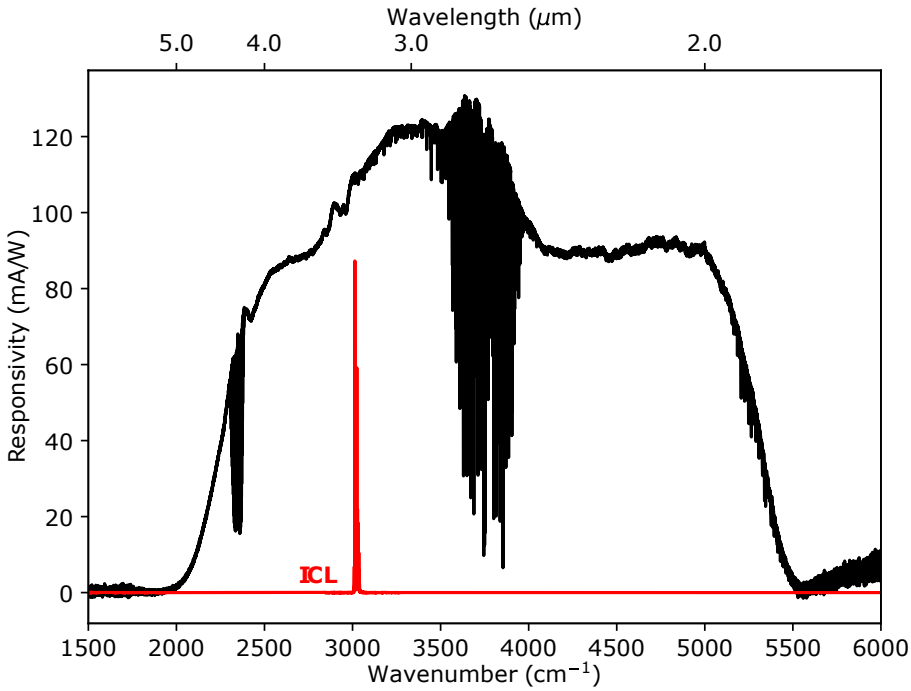

Figure 4.5: Recorded responsivity of the 1 mm sized mesa of ICIP2. Despite that the absorber length of ICIP2 is reduced to one third compared to ICIP1 the responsivity is still high. Figure taken with permission from [3].

Direct modulation of an interband cascade laser:

The frequency response of an ICIP can be simply measured by detecting directly the RF modulated radiation of an ICL. Therefore, an ICL emitting at a wavelength of 4.3 µm was processed in a ridge waveguide configuration featuring a long gain section and a smaller modulation section. In order to obtain the net RF response of just the ICIP detector, the RF response of the ICL was first characterized using a QCD, which is working much faster than the ICL, at the same wavelength. Next, the RF response of the setup (cables, bias tee and equipment) was measured. These two obtained responses were at the end subtracted from the measured ICIP response.

The complete setup for this measurement is illustrated in Fig. 4.6. The gain and modulation sections of the ICL were connected to a DC current source, the modulation section was additionally connected to a RF signal generator. The ICL was then modulated from 10 MHz up to 20 GHz. A multimeter measured the generated DC signal of the ICIP, and the RF signal was evaluated through a spectrum analyzer. Additionally, to minimize the cross-talk which is generated by the equipment, a chopper was placed in the beam path

between the ICL and the ICIP. Consequently, side beatings are generated next to the fundamental modulated beating, at frequencies separated by the multiple of the chopper frequency. The RF response was then calculated from the arithmetic mean value of the two closest side beatings.

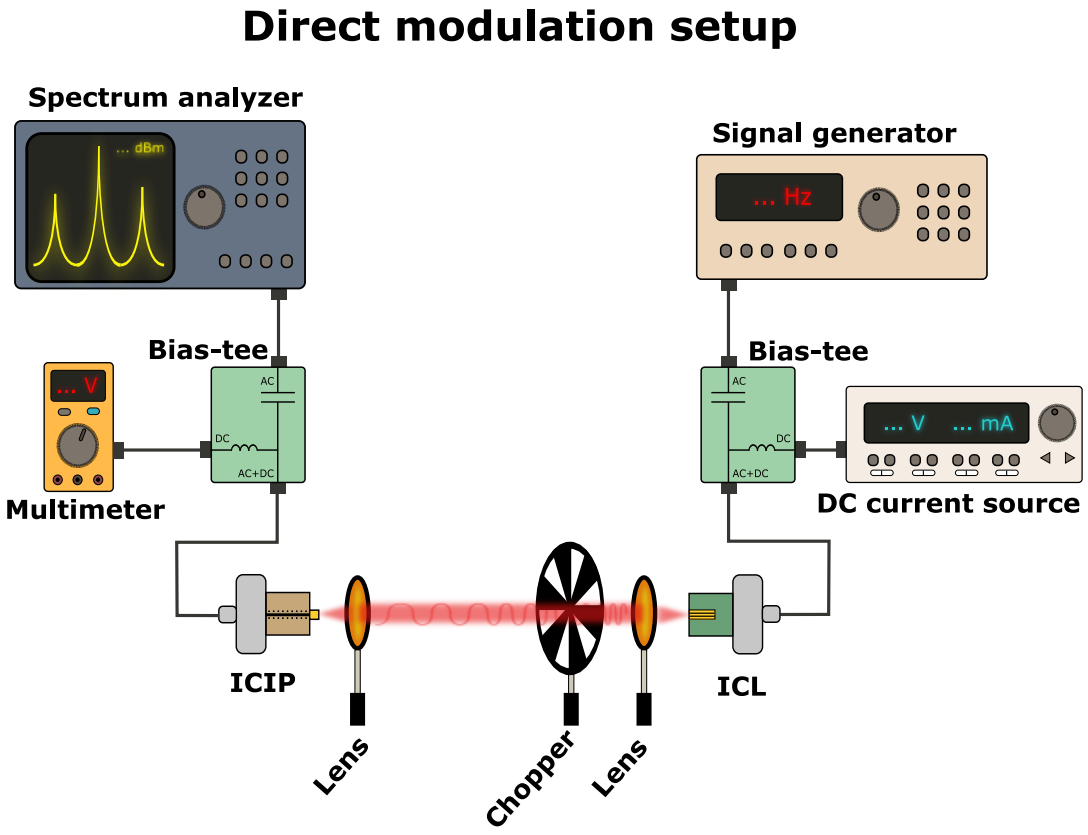

Figure 4.6: Illustrated setup of the RF response measurements of the ICIP devices. The directly modulated light emitted from an ICL gets detected by an ICIP and furthermore evaluated using a spectrum analyzer. A chopper was used to generate side beatings and avoid cross-talk.

The results of this direct modulation measurement were all achieved with the ICIPs fabricated in the scope of the PhD work of [3] and are presented in Fig.4.7 and Fig.4.8. The left column shows the results of the ICIP1 design and the right one of the ICIP2 design. In Fig.4.7 the dependency of the frequency response on the bias voltage is shown by sweeping the bias from -0.5 to 5 V. The 3-dB cutoff frequency for the net response

of a 20 µm ICIP1 mesa at 5 V bias lies at 1.3 GHz. For the ICIP2 design with the same parameters the 3-dB cutoff frequency is increased to 1.8 GHz. The absorbers of ICIP2 are thinner compared to ICIP1 and consequently the electrical capacitance is higher, but the total transit time of the generated carriers is shorter. Therefore, a flatter frequency response can be achieved with this design. In Fig.4.8 the influence of the device diameter on the RF response is presented at three different biases. The electrical capacitance is influenced by the size of the mesas Eq.2.11, and the measurements confirmed a general flatter response for smaller mesas. Unfortunately, the losses of the setup were too high to obtain reliable data to extract meaningful carrier transport times, especially for higher frequencies. Hence, an alternative measurement technique using an optical parametric oscillator (OPO) was applied.

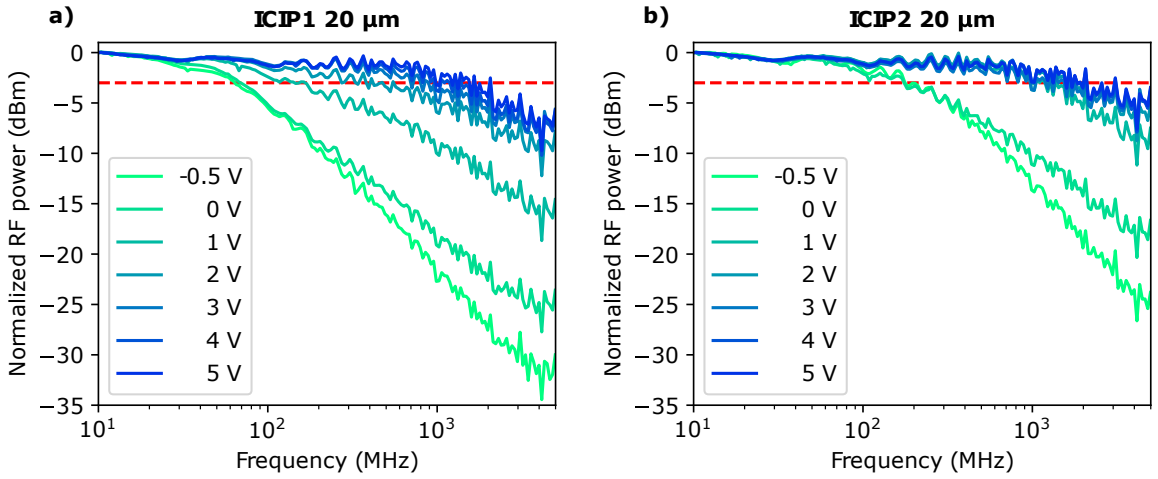

Figure 4.7: Net frequency response of the 20 µm mesa devices of **a)** the ICIP1 and **b)** ICIP2 design at different bias voltages. A 3-dB cutoff frequency of 1.3 GHz for ICIP1 and 1.8 GHz for ICIP2 was achieved at 5 V. The red dashed horizontal line marks the 3-dB power cutoff. Figure taken with permission from [3].

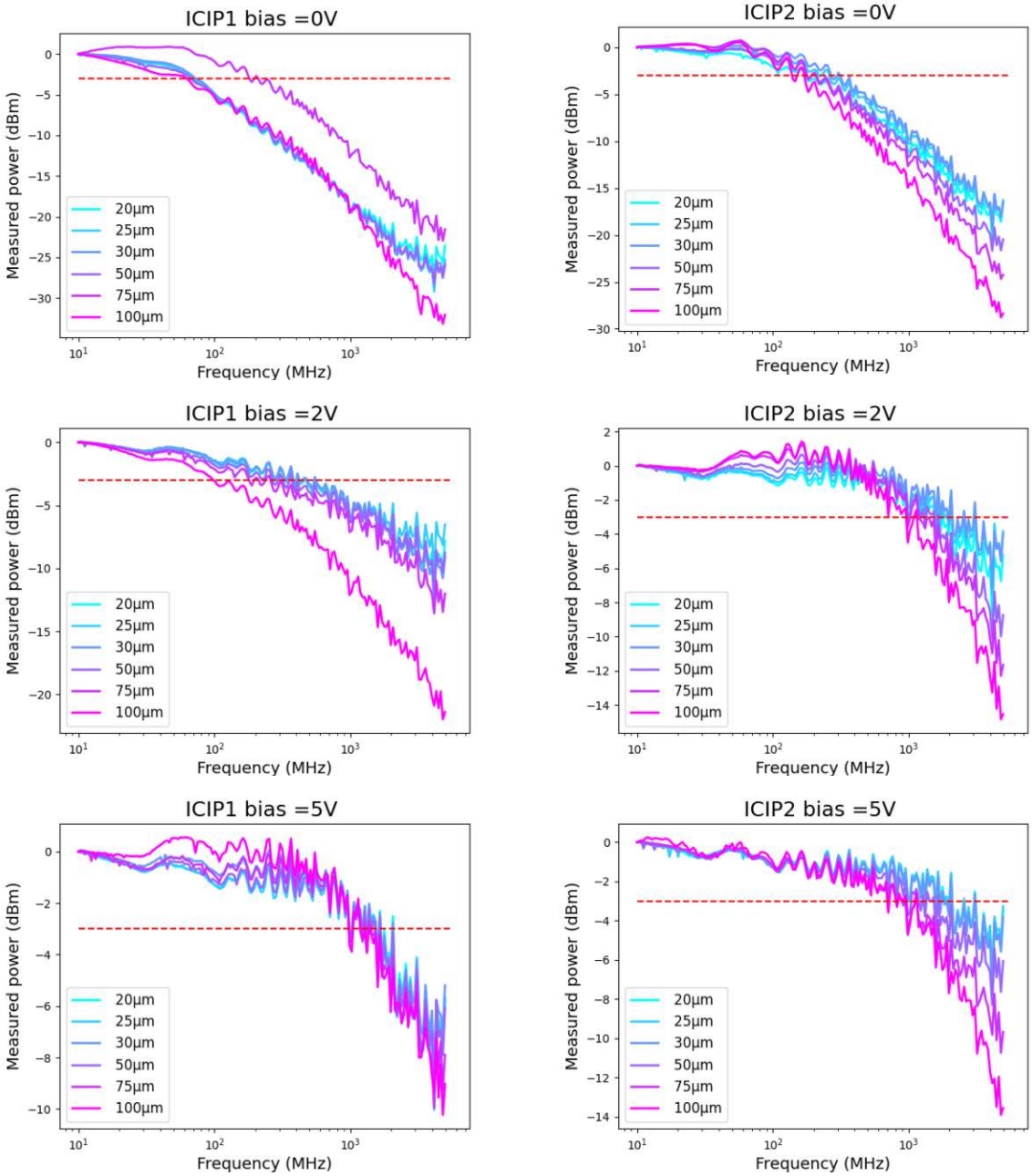

Figure 4.8: Net frequency response for the two different absorber designs ICIP1 and ICIP2 in the left and right column respectively. Different sized devices are plotted at three different bias voltages. The red dashed horizontal line marks the 3-dB power cutoff.

Impulse and frequency response with an optical parametric oscillator (OPO): Another approach to characterize the frequency response of the ICIPs was attempted because the results of the directly modulated ICL experiments were unsatisfactorily for higher frequencies. For this new approach the RF response of the ICIPs is calculated from the impulse response of the devices. In order to generate ultra-short pulses, in the range of femtoseconds and with high output power, an optical parametric oscillator (OPO) was required. The OPO is a resonator in which optical gain is achieved from parametric amplification of a pump source, in usually a nonlinear crystal, as illustrated on the right side of Fig.4.9.

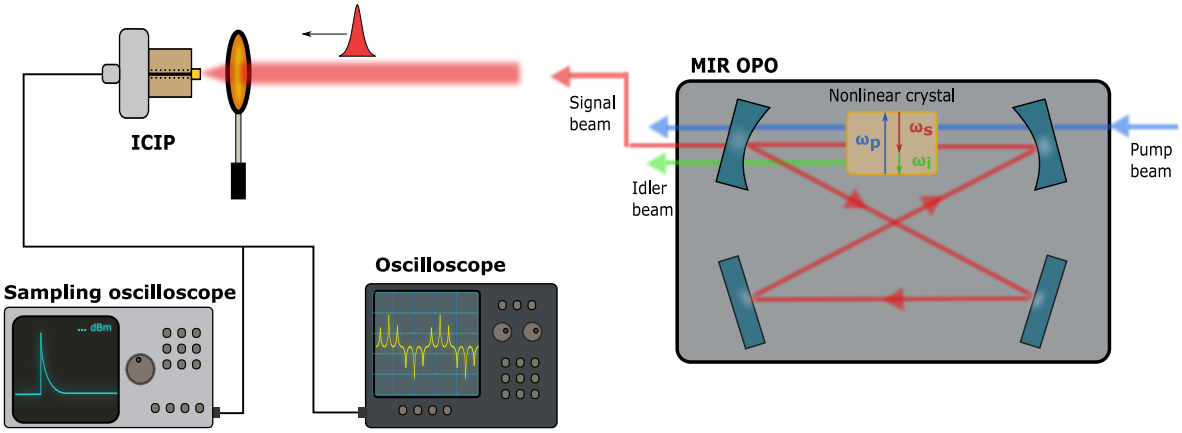

Figure 4.9: Illustration of the experimental setup for the impulse response measurement of an ICIP. The optical parametric oscillator (OPO) consists of a nonlinear component which converts the pump beam (blue) down to a signal (red) and idler (green) beam. A pulsed high power signal beam is then generated by parametric amplification and out-coupled from the OPO. The femtosecond pulses are then focused onto the uncooled ICIP. The impulse response of the detector is measured using a sampling oscilloscope and an oscilloscope.

The pump frequency ω_p gets converted by means of second-order nonlinear optical interaction into two lower output frequencies which are called signal ω_s and idler ω_i under the condition that $\omega_s + \omega_i = \omega_p$. By changing the pump frequency or the phasematching properties of the nonlinear optical crystal the output frequencies can be tuned over a broad spectral range. Thankfully, all the needed equipment and facilities were placed at disposal from the group of Ursula Keller from the Institute for Quantum Electronics at ETH Zürich and the following measurements were performed with the help of Jonas

Heidrich. The provided OPO had a pulse repetition rate of 80.2 MHz and a tunable average output power up to 15 mW and above. The shape of the generated pulse was assumed to have a $sech^2$ form with a pulse width of around 100 fs. The generated pulsed beam, which can be regarded as a good approximation for δ-pulses regarding the ICIP detection speed, was then focused onto the uncooled ICIP and the induced impulse response was recorded by a sampling oscilloscope and an oscilloscope, as shown on the left side of Fig.4.9. The following measurements were all performed with the newly designed ICIPs, which were realized in scope of this work (section 3).

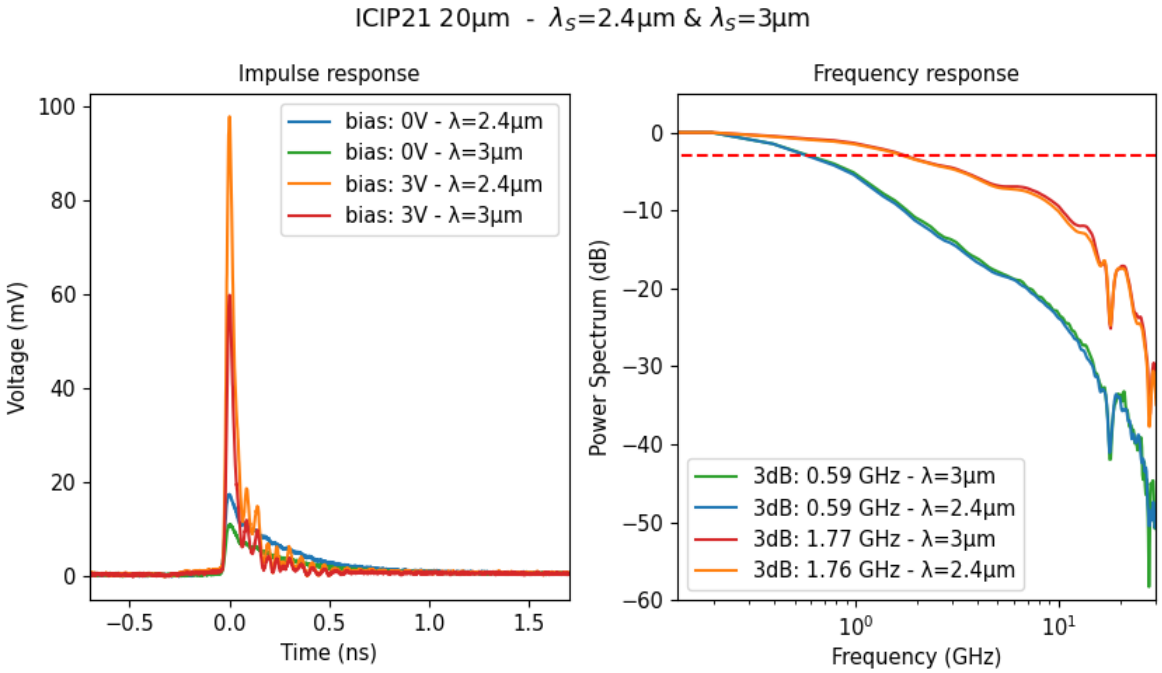

Figure 4.10: Impulse response on the left side and RF response on the right side of ICIP21 for two different input wavelengths at 0 V and 3 V bias. The signal beam of the OPO was switched between $\lambda_s = 2.4\,\mu m$ and $\lambda_s = 3\,\mu m$ with a constant 1 mW output power. A dependence of the peak response on the wavelength is seen on the left side for the same bias, however the shape of the response stays the same, hence, no change in the frequency response occurs.

First, the dependence of the impulse and frequency response on the input wavelength was investigated. Therefore, the wavelength of the signal beam was switched between 2.4 µm and 3 µm with a constant 1 mW output power and the response was measured at

0 V and 3 V bias, respectively. Although the responsivity of ICIP2, which was described in the previous section, is around 30% lower at 2.4 µm compared to 3 µm, a higher peak response arose at 2.4 µm, as presented in Fig 4.10. A possible explanation for the lower response at 3 µm might be, that the beam gets attenuated since a CO_2 absorption band edge is located around this wavelength. The frequency response is however not influenced by the input wavelength since the width of the impulse response stays unchanged. For all the following measurements the OPO's signal beam was chosen to be at a wavelength of 2.4 µm.

Next, the high-speed performances of three different ICIP structures are analyzed. The frequency response of the ICIP is given by the one-dimensional discrete Fourier transform of the impulse response, FFT|(impulse response)|^2. The wavelength of the OPOs signal beam was set to λ_s=2.4 µm with a constant 1 mW output power. On the left side of Fig. 4.11 and Fig. 4.12 the normalized impulse response of ICIP11, ICIP22 and ICIP21 is shown at different biases ranging from −0.5 V to 5 V. On the right side the normalized frequency response is seen, whereas the red dashed line marks the 3-dB power cutoff. The oscillations seen in the tail of the impulse response are probably caused by reflections. The incomplete impulse response at low bias leads to a slight overestimation of the 3-dB power cutoff. Moreover, the results do not include the losses of the cables and the bias tee and are therefore expected to be even better. The influence of the bias is clearly visible: by increasing the bias the full width at half maximum (FWHM) of the impulse response decreases resulting in a higher cutoff frequency. A strong dependence of the cutoff frequency to the bias is seen up to 3 V, for higher biases this influence decreases. The 3-dB cutoff frequency of ICIP11 at 5 V bias lies at 710 MHz, which is half of the value obtained from the direct modulation measurements. Unfortunately, only one ICIP with the longer absorber design 1 was measured, hence, no statistical comparison of the frequency response of this structure was drawn. For the ICIP21 and ICIP22 the 3-dB cutoff frequency lies at 1.95 GHz and 1.76 GHz, respectively, which is in good agreement with the direct modulation measurements. Furthermore, the frequency response obtained from this measurement method clearly improved in smoothness for higher frequencies compared to the previous results.

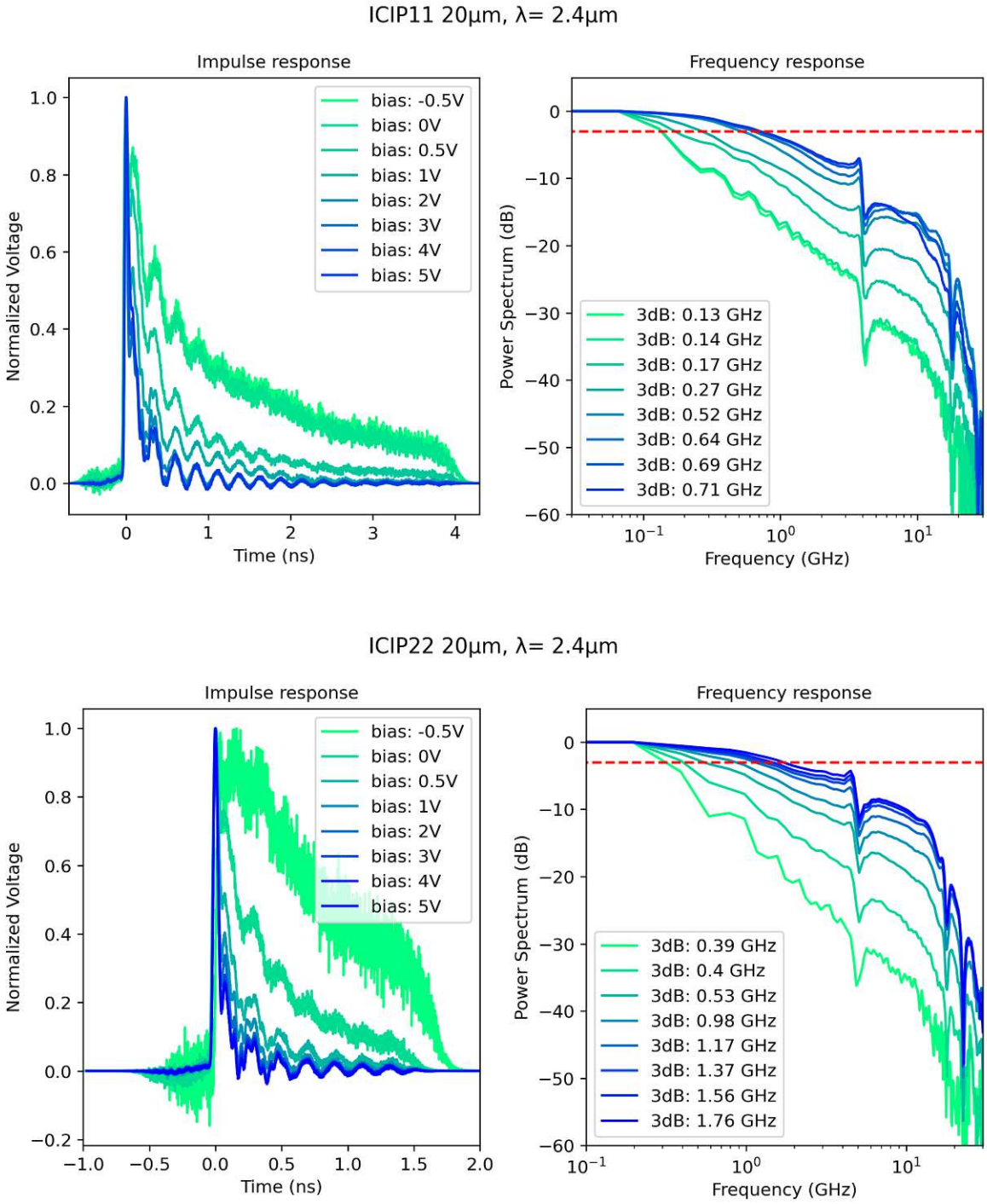

Figure 4.11: Normalized impulse response and frequency response of ICIP11 at the top and ICIP22 at the bottom for different applied biases. The red dashed line marks the 3-dB power cutoff. The input beam had a wavelength of 2.4 µm and a power of 1 mW. The incomplete impulse response at low bias leads to a slight overestimation of the 3-dB power cutoff.

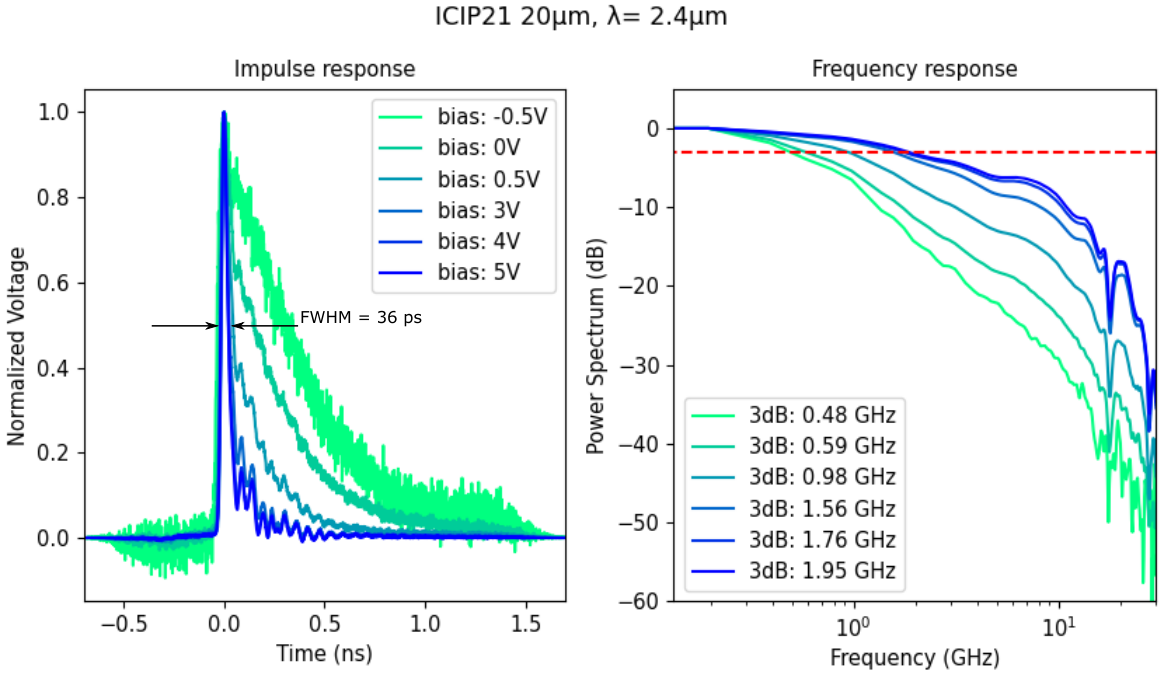

Figure 4.12: Normalized impulse response and frequency response of ICIP21 on the left and right side, respectively. For 5 V bias the full width at half maximum (FWHM) of the impulse response is 36 ps and the 3-dB cutoff of the frequency response lies at 1.95 GHz. The incomplete impulse response at low bias leads to a slight overestimation of the 3-dB power cutoff.

Finally, the saturation behavior of the devices was studied. The impulse response of ICIP21 was measured at incident pulse powers ranging from 0.5 to 15 mW at 0 V and 3 V bias, as shown in Fig.4.13. With increasing incident power, the peak response increases and by applying a bias the FWHM of the response decreases. Next, the dependency of the DC current and the peak response over the incident pulse energy of ICIP21 was analyzed. The incident pulse energy can be simply calculated from $E = \frac{P_{avg}}{f_{rep}}$ and the net DC current is calculated from the difference of the measured DC current and the DC offset. On the left side of Fig.4.14 the experimental data of the net current, and on the ride side the experimental data of the peak response for 0 V and 3 V bias are marked with dots. The saturation energy E_{sat} is defined as the energy at which the absorption is reduced to half of its initial low-power absorption.

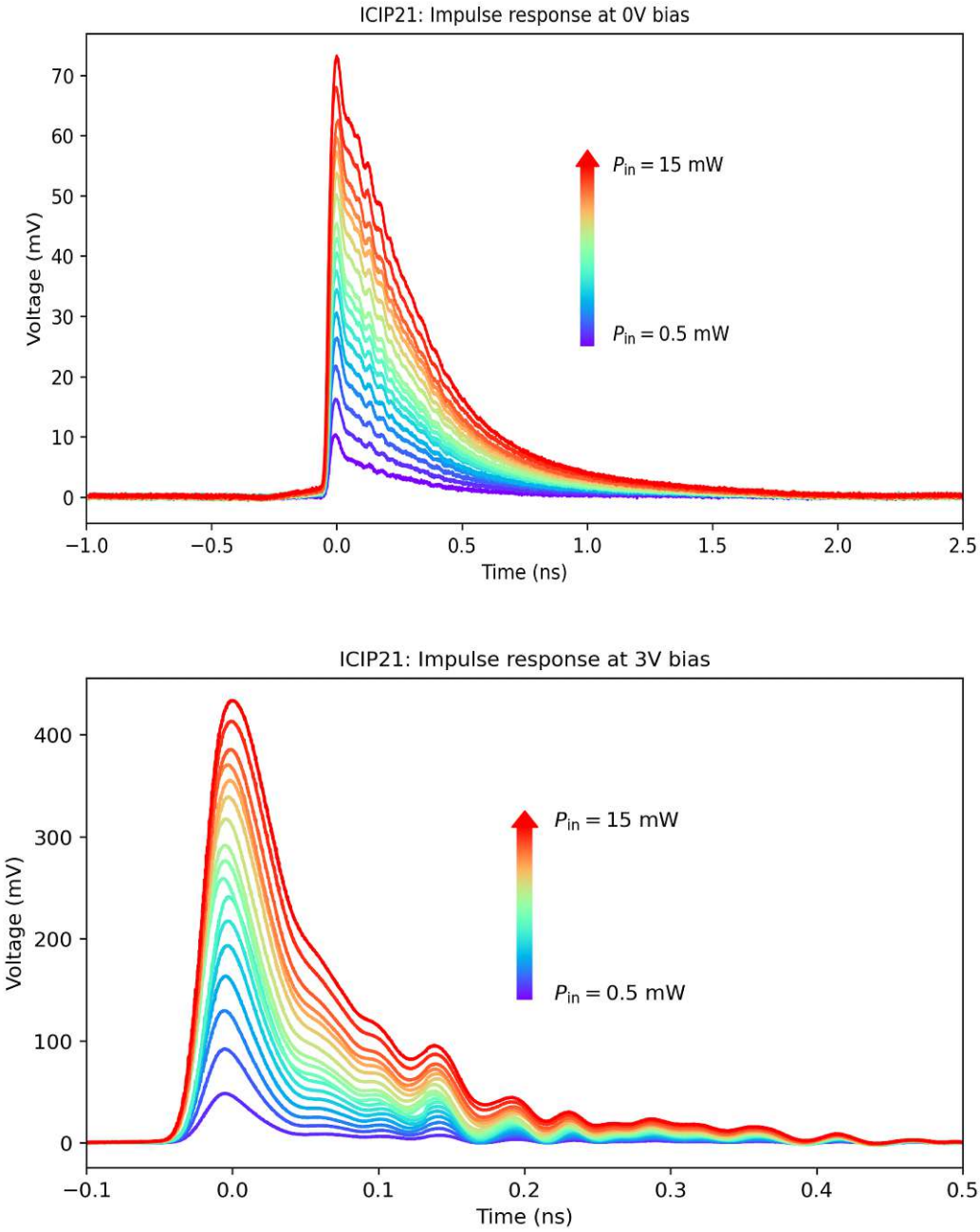

Figure 4.13: The impulse response of ICIP21 for different incident pulse energies ranging from 0.5 to 15 mW. Top measurements were taken at 0 V bias and bottom at 3 V bias.

To quantify the observed macroscopic saturation behavior of the ICIP a simplified model was used to fit the saturation behavior in generated peak voltage and DC current:

$$V_{peak} = \frac{\alpha_0}{(1 + \frac{E_{in}}{E_{sat}})\frac{E_{in}}{E_{sat}}} + V_{offset} \tag{4.2}$$

$$I_{DC} = \frac{\alpha_0}{(1 + \frac{E_{in}}{E_{sat}})\frac{E_{in}}{E_{sat}}} + I_{offset} \tag{4.3}$$

α_0, which is the initial low-power absorption, was assumed to be constant in order to obtain the saturation energy. The results of the fit can be seen as solid lines in Fig4.14. With increasing bias voltage the saturation energy also increases for the DC current and for the peak response, reaching values of 228 pJ (23 mW) and 83 pJ (6.5 mW). It has been reported in literature, that the absorption coefficient decreases with intensity, because of the depletion of available carriers in the two-dimensional quantum wells [47, 48, 49]. In order to obtain the equilibrium saturation energy, this measurement needs to be performed under continuous wave or longer pulsed radiation, since the carrier dynamics in this structure are much slower than a femtosecond pulse.

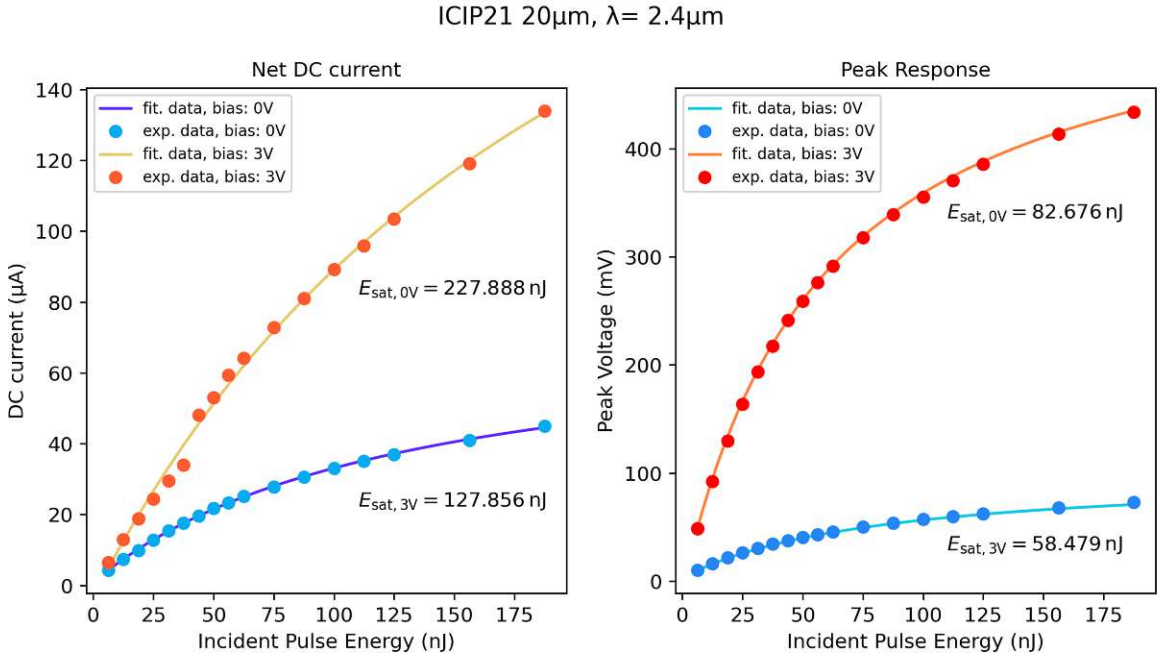

Figure 4.14: The calculated net DC current on the left side and on the right side the peak responsivity of ICIP21 depending on the incident beam power. Top measurements were taken at 0 V bias and bottom at 3 V bias.

4.3 High-speed applications

This last section presents two examples of high-speed applications for the ICIPs. The experiments were conducted with the ICIPs of design 1 with a diameter of 100 µm, which were realized in the work of H. Knötig [3].

Frequency-comb characterization:
In 2014, Burghoff et al. [50] developed shifted wave interference Fourier transform spectroscopy (SWIFTS). Ever since, it has been an established method to obtain information about the temporal waveform and phase-coherence of semiconductor frequency combs and was already applied numerous times [51, 52].
The underlying principle of SWIFTS is the detection of the frequency comb beating at its roundtrip frequency. Each comb line beats with its neighbors at their difference frequency causing a modulation of the laser intensity at the beating frequency, which is the so-called laser beatnote. The beatnote frequency typically sits around 10 GHz for infrared ICL or QCL frequency combs of about 4 mm waveguide length, and can be measured using fast detectors. ICIPs are well suited candidates for this task, since they generate high signals, can be operated at room temperature and have a broad spectral bandwidth.
The amplitudes and phases of the individual intermodal beatings, which lie between two adjacent comb lines, were detected. Therefore, the comb is shone through a FTIR spectrometer, which allows to discriminate the frequencies of the individual comb lines. The ICIP measures the average power and the beatnote. In order to obtain the two quadratures of the beatnotes X and Y, which represent the phase and amplitude of the beatnote a lock-in amplifier is used to demodulate the beatnote after the FTIR using the beatnote before the FTIR as phase reference. In this way, the intensity and complex SWIFTS interferograms are recorded. Next, by applying a Fourier transformation on the interferograms the intensity and complex SWIFTS spectra can be obtained. A 2π phase difference is displayed over the entire spectral range, which corresponds to exactly one cavity roundtrip. Hence, every part of the spectrum is emitted at a different time during a roundtrip period, which leads to frequency modulation (FM) behavior, showing almost constant intensity in the time domain. The results of a SWIFTS measurement with FM behavior, performed in collaboration with F.Pilat, are shown in Fig.4.15. The

ICIPs provided a remarkable performance compared to the previously used detectors, even when operating at room temperature.

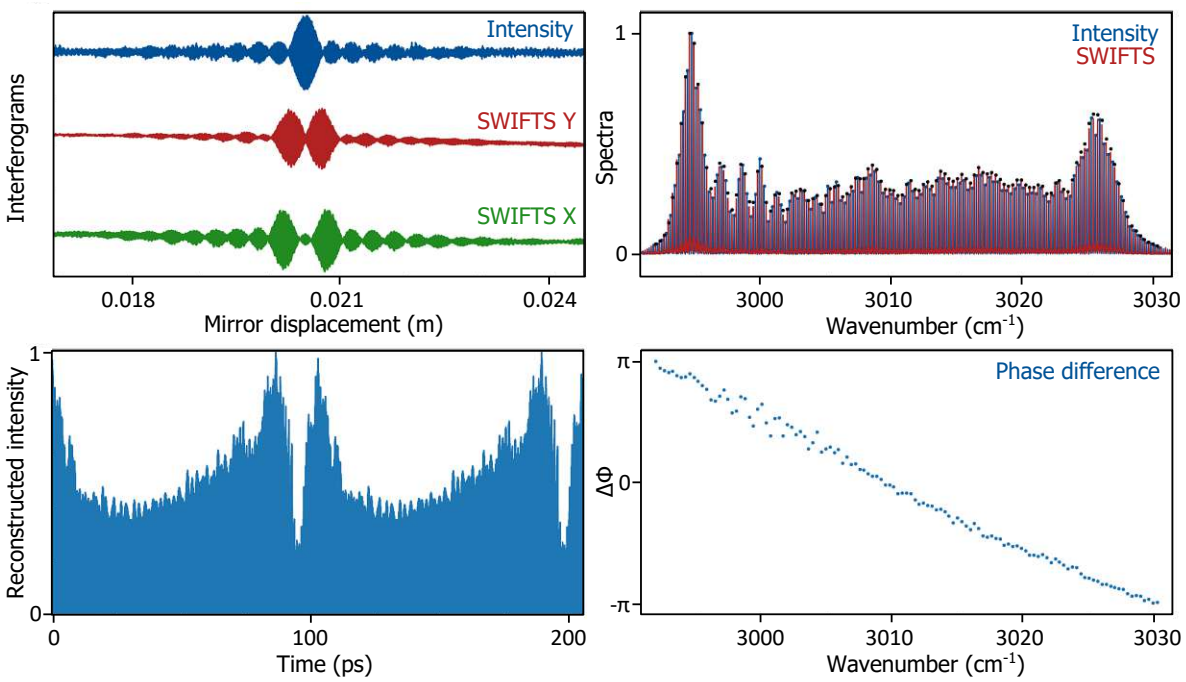

Figure 4.15: SWIFTS characterization of an ICL frequency comb exhibiting FM behavior. **Top:** Intensity and quadrature SWIFTS interferograms (left), corresponding intensity and complex SWIFTS spectra (right). **Bottom:** Reconstructed intensity waveform and intermodal phase differences. With permission from [3].

Free-space optical communication:

Another promising field of application for fast ICIPs is free-space communication, where several experiments have been conducted lately [53, 54]. A full interband system was arranged, composed of an ICIP and a directly modulated ICL, which is emitting at 4.1 µm and is optimized for RF injection [55], by the group of Frédéric Grillot from the Institut Polytechnique de Paris. The bandwidth of the ICIP can be tuned by applying a bias as seen in Fig 4.16 a), hence a 3-dB bandwidth of 1.7 GHz is achieved at a bias of 5 V. However, since the 3-dB bandwidth of the ICIP lies at around two thirds of the bandwidth of the ICL, this system is limited by the performance of the detector. Nevertheless, transmission for a data rate of 12 Gbits/s has been demonstrated using a 2

level modulation scheme over a distance of 2 m. In Fig.4.16 b) the obtained eye diagram is displayed. An on-off keying format is used generating a bit error rate (BER) of 1.5 x 10^{-2}. In literature free-space optical communication experiments have been conducted using an ICL and an MCT detector with a maximum transmission rate of 300 Mbits/s [56]. For a QCL at 4.65 µm combined also with an MCT detector transmission rates of up to 6 Gbits/s were reported [57]. Therefore, the results obtain with the ICIP are very promising for future applications.

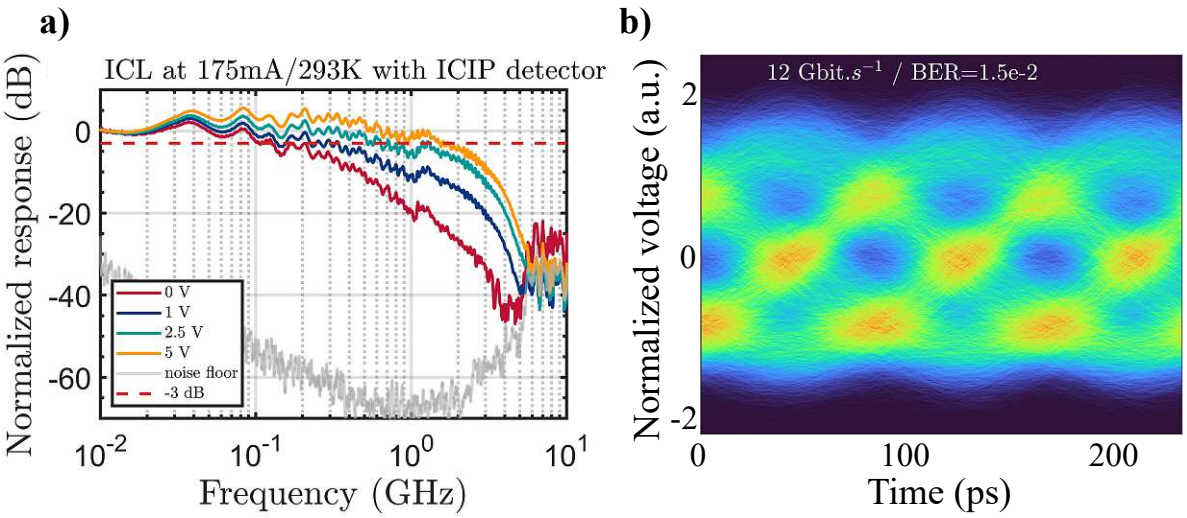

Figure 4.16: a) ICL and ICIP system frequency response when applying variable bias up to a maximum of 5 V. **b)** Characteristic eye diagram of an on-off keying format after free-space propagation of around 2 meters with a transmission rate of 12 Gbits/s. Figure taken with permission from [53, 54].

5 Conclusion and Outlook

Interband cascade infrared photodetecots are promising mid-IR detectors for fast and broad wavelength detection at room temperature. They are based on ICLs and combine interband optical transitions with fast intraband transport. Moreover ICIPs benefit from low-noise, high-speed and high sensitivity characteristics and aspire to successfully compete with the widely used mid-infrared detectors such as MCTs, QWIPs and QCDs. The goal of this thesis was to investigate the high-speed performance of ICIPs, to fabricate optimized devices and to study their limitations.

Two different absorber thicknesses were presented in this work, where the shorter absorber outperformed the longer one in all high-speed measurements. These results consolidate the assumption that more stages, each composed of a short absorber increase the high-speed performance of the device. The fastest multistage ICIP detector in literature is currently composed of five cascade stage with an absorber thickness of 240 nm [31].
A new design for electrically contacting the smaller sized mesas with a diameter below 100 µm was successfully developed and implemented during this work. The use of SU-8 photoresist to extend the contact pad enabled the packaging and bonding of the smallest sized mesas without deteriorating their high-speed performance.

The main advantages of ICIPs, is their broad spectral coverage along with their promising potential for high-speed applications. These two features are combined in ICIPs but can not be found in the other state-of-the-art mid-infrared detectors, making them perfect candidates for a variety of applications. Applications, like light detection and ranging (LIDAR) or laser characterization are just two examples where ICIPs are well suited for. The relevance of this work is supported by the two application examples of the devices realized in the work of H. Knötig [3]. Where the ICIPs were successfully implemented for the characterization of frequency combs during SWIFTS measurements and showed outstanding results in free-space communication experiments.

Two different measurement setups were present during the course of this thesis where the measurements taken with the OPO showed a dramatic improvement in the high fre-

quency domain. The collected data furthermore enabled ongoing investigations of the tunneling rates, extraction rates and other fundamental carrier lifetimes within the superlattice absorber. First results hint at two distinct decay times, possibly connected to the different contributions of electrons and holes. Consequently, by adapting the absorber design to the obtained rates and lifetimes, the high-speed performance of the ICIPs could be improved even further.

Also essential to mention are the prromising results recently achieved with InAs/InAsSb type-II superlattice ICIPs [58]. Since InAs/GaSb superlattice absorbers suffer from low carrier lifetimes due to Shockley-Read-Hall recombination associated with native defects related to GaSb this Ga-free superlattice could potentially circumvent this limitation and greatly improve ICIP performance. Recently a 3-dB cutoff frequency of 12.8 GHz was reported for a detector featuring a single 900 nm thick absorber [32]. Without a doubt, the upcoming years will reveal exciting advances for superlattice ICIPs and I am confident they will be established as a standard detector for the mid-infrared region in the future.

Abbreviations

EBR edge bead removal
FM frequency modulation
FPA focal plane arrays
FTIR Fourier-transform infrared spectrometer
FWHM full width at half maximum
GSG ground-source-ground
ICIP interband cascade infrared photodetector
ICL interband cascade laser
LWIR long-wavelength infrared region
MBE molecular beam epitaxy
MCT mercury cadmium telluride
MWIR mid-wavelength infrared region
NWIR near-wavelength infrared region
OPO optical parametric oscillator
PCB printed circuit board
PECVD plasma enhanced chemical vapor deposition
QCD quantum cascade detector
QW quantum well
QWIP quantum well infrared photodetector
RF radio frequency
RIE reactive ion etching
RT room temperature
RTA rapid thermal annealing
SNR signal to noise ratio
T2SL type-II superlattice
VLWIR very long-wavelength infrared region

References

[1] H. Lotfi, L. Li, L. Lei, Y. Jiang, R. Q. Yang, J. F. Klem, and M. B. Johnson, "Short-wavelength interband cascade infrared photodetectors operating above room temperature," *Journal of Applied Physics*, vol. 119, p. 023105, 1 2016.

[2] A. Rogalski, "History of infrared detectors," *Opto-Electronics Review*, vol. 20, pp. 279–308, 1 2012.

[3] H. M. Knötig, "Interband cascade lasers and detectors: From active region design to devices," Dissertation, Technische Universität Wien, 2022.

[4] J. Hillbrand, "Microwave photonics using semiconductor laser frequency combs," 2020.

[5] D. Ting, S. Rafol, A. Khoshakhlagh, A. Soibel, S. Keo, A. Fisher, B. Pepper, C. Hill, and S. Gunapala, "Inas/inassb type-ii strained-layer superlattice infrared photodetectors," *Micromachines*, vol. 11, p. 958, 10 2020.

[6] I. Vurgaftman, M. P. Lumb, and J. R. Meyer, *Bands and photons in III-V semiconductor quantum structures*. Oxford University Press, first edition. ed., 2021.

[7] R. T. Hinkey and R. Q. Yang, "Theory of multiple-stage interband photovoltaic devices and ultimate performance limit comparison of multiple-stage and single-stage interband infrared detectors," *Journal of Applied Physics*, vol. 114, p. 104506, 9 2013.

[8] W. D. Lawson, S. Nielsen, E. H. Putley, and A. S. Young, "Preparation and properties of hgte and mixed crystals. of hgte-cdte," 1959.

[9] S. C. Shen, "Comparison and competition between mct and qw structure material for use in ir detectors," 1994.

[10] C. Verie and M. Sirieix, "Gigahertz cutoff frequency capabilities of cdhgte photovoltaic detectors at 10.6 μ," *IEEE Journal of Quantum Electronics*, vol. 8, pp. 180–184, 2 1972.

[11] A. Rogalski, "Hgcdte infrared detector material: history, status and outlook," *Reports on Progress in Physics*, vol. 68, pp. 2267–2336, 10 2005.

[12] S. C. Shen and Z. S. B. Y. Road, "I mct versus quantum well structures i i for ir detectors," 1993.

[13] L. Lei, L. Li, H. Lotfi, H. Ye, R. Q. Yang, T. D. Mishima, M. B. Santos, and M. B. Johnson, "Midwavelength interband cascade infrared photodetectors with superlattice absorbers and gain," *Optical Engineering*, vol. 57, p. 1, 9 2017.

[14] B. F. Levine, "Quantum-well infrared photodetectors," *Journal of Applied Physics*, vol. 74, pp. R1–R81, 10 1993.

[15] H. Schneider and H. C. Liu, "Quantum well infrared photodetectors physics and applications."

[16] H. C. Liu, J. Li, M. Buchanan, and Z. R. Wasilewslu, "High-frequency quantum-well infrared photodetectors measured by microwave-rectification technique," 1996.

[17] P. D. Grant, R. Dudek, M. Buchanan, and H. C. Liu, "Room-temperature heterodyne detection up to 110 ghz with a quantum-well infrared photodetector," *IEEE Photonics Technology Letters*, vol. 18, pp. 2218–2220, 11 2006.

[18] S. Gunapala, S. Bandara, J. Liu, C. Hill, S. Rafol, J. Mumolo, J. Trinh, M. Tidrow, and P. LeVan, "Development of mid-wavelength and long-wavelength megapixel portable qwip imaging cameras," *Infrared Physics & Technology*, vol. 47, pp. 67–75, 10 2005.

[19] D. Hofstetter, M. Beck, and J. Faist, "Quantum-cascade-laser structures as photodetectors," *Applied Physics Letters*, vol. 81, pp. 2683–2685, 10 2002.

[20] L. Gendron, M. Carras, A. Huynh, V. Ortiz, C. Koeniguer, and V. Berger, "Quantum cascade photodetector," *Applied Physics Letters*, vol. 85, pp. 2824–2826, 10 2004.

[21] J. Hillbrand, L. M. Krüger, S. D. Cin, H. Knötig, J. Heidrich, A. M. Andrews, G. Strasser, U. Keller, and B. Schwarz, "High-speed quantum cascade detector characterized with a mid-infrared femtosecond oscillator," *Optics Express*, vol. 29, p. 5774, 2 2021.

[22] D. Hofstetter, M. Graf, T. Aellen, J. Faist, L. Hvozdara, and S. Blaser, "23ghz operation of a room temperature photovoltaic quantum cascade detector at 5.35μm," *Applied Physics Letters*, vol. 89, p. 061119, 8 2006.

[23] R. Paschotta, "Thermal detectors," *RP Photonics Encyclopedia*.

[24] S. P. Langley, *The" bolometer"*. The Society, 1881.

[25] A. Graf, M. Arndt, M. Sauer, and G. Gerlach, "Review of micromachined thermopiles for infrared detection," *Measurement Science and Technology*, vol. 18, p. R59, may 2007.

[26] A. Hossain and M. Rashid, "Pyroelectric detectors and their applications," *IEEE Transactions on Industry Applications*, vol. 27, no. 5, pp. 824–829, 1991.

[27] R. Q. Yang, "Infrared laser based on intersubband transitions in quantum wells," *Superlattices and Microstructures*, vol. 17, pp. 77–83, 1 1995.

[28] R. Q. Yang, Z. Tian, Z. Cai, J. F. Klem, M. B. Johnson, and H. C. Liu, "Interband-cascade infrared photodetectors with superlattice absorbers," *Journal of Applied Physics*, vol. 107, p. 054514, 3 2010.

[29] Y. Chen, X. Chai, Z. Xie, Z. Deng, N. Zhang, Y. Zhou, Z. Xu, J. Chen, and B. Chen, "High-speed mid-infrared interband cascade photodetector based on inas/gaassb type-ii superlattice," *Journal of Lightwave Technology*, vol. 38, pp. 939–945, 2 2020.

[30] R. Q. Yang and R. T. Hinkey, "Ultimate detectivity of multiple-stage interband cascade infrared photodetectors," *Applied Physics Letters*, vol. 118, p. 241101, 6 2021.

[31] Z. Xie, J. Huang, X. Chai, Z. Deng, Y. Chen, Q. Lu, Z. Xu, J. Chen, Y. Zhou, and B. Chen, "High-speed mid-wave infrared interband cascade photodetector at room temperature," *Optics Express*, vol. 28, p. 36915, 11 2020.

[32] J. Huang, Z. Shen, Z. Wang, Z. Zhou, Z. Wang, B. Peng, W. Liu, Y. Chen, and B. Chen, "High-speed mid-wave infrared uni-traveling carrier photodetector based on inas/inassb type-ii superlattice," *IEEE Electron Device Letters*, vol. 43, pp. 745–748, 5 2022.

[33] W. Huang, L. Lei, L. Li, J. A. Massengale, R. Q. Yang, T. D. Mishima, and M. B. Santos, "Current-matching ¡i¿versus¡/i¿ non-current-matching in long wavelength interband cascade infrared photodetectors," *Journal of Applied Physics*, vol. 122, p. 083102, 8 2017.

[34] L. Lei, L. Li, H. Ye, H. Lotfi, R. Q. Yang, M. B. Johnson, J. A. Massengale, T. D. Mishima, and M. B. Santos, "Long wavelength interband cascade infrared photodetectors operating at high temperatures," *Journal of Applied Physics*, vol. 120, p. 193102, 11 2016.

[35] H. Lotfi, L. Li, H. Ye, R. T. Hinkey, L. Lei, R. Q. Yang, J. C. Keay, T. D. Mishima, M. B. Santos, and M. B. Johnson, "Interband cascade infrared photodetectors with long and very-long cutoff wavelengths," *Infrared Physics & Technology*, vol. 70, pp. 162–167, 5 2015.

[36] H. Lotfi, L. Li, L. Lei, H. Ye, S. M. S. Rassel, Y. Jiang, R. Q. Yang, T. D. Mishima, M. B. Santos, J. A. Gupta, and M. B. Johnson, "High-frequency operation of a mid-infrared interband cascade system at room temperature," *Applied Physics Letters*, vol. 108, p. 201101, 5 2016.

[37] nanoplus, Nanosystems and Technologies GmbH, www.nanoplus.com.

[38] N. Ghalichechian and K. Sertel, "Permittivity and loss characterization of su-8 films for mmw and terahertz applications," *IEEE Antennas and Wireless Propagation Letters*, vol. 14, pp. 723–726, 2015.

[39] P. Abgrall, V. Conedera, H. Camon, A.-M. Gue, and N.-T. Nguyen, "Su-8 as a structural material for labs-on-chips and microelectromechanical systems," *ELECTROPHORESIS*, vol. 28, pp. 4539–4551, 12 2007.

[40] A. Mata, A. J. Fleischman, and S. Roy, "Fabrication of multi-layer su-8 microstructures," *Journal of Micromechanics and Microengineering*, vol. 16, pp. 276–284, 2 2006.

[41] MicroChem, "Su-8 2000 permanent epoxy negative photoresist processing guidelines for: Su-8 2000.5, su-8 2002, su-8 2005, su-8 2007, su-8 2010 and su-8 2015."

[42] H. Lee, K. Lee, B. Ahn, J. Xu, L. Xu, and K. W. Oh, "A new fabrication process for uniform su-8 thick photoresist structures by simultaneously removing edge bead and air bubbles," *Journal of Micromechanics and Microengineering*, vol. 21, p. 125006, 12 2011.

[43] H. W. Park, H. J. Kim, J. H. Roh, J.-K. Choi, and K.-R. Cha, "Simple and cost-effective method for edge bead removal by using a taping method," *Journal of the Korean Physical Society*, vol. 73, pp. 1473–1478, 11 2018.

[44] M. Shaw, D. Nawrocki, R. Hurditch, and D. Johnson, "Improving the process capability of su-8," *Microsystem Technologies*, vol. 10, pp. 1–6, 12 2003.

[45] E. A. Plis, M. N. Kutty, and S. Krishna, "Passivation techniques for inas/gasb strained layer superlattice detectors," *Laser & Photonics Reviews*, vol. 7, pp. 45–59, 1 2013.

[46] N. W. Khan, F. Rothmayr, A. Bader, F. Hartmann, R. Weih, J. Koeth, and S. Höfling, "Process optimization of sulfur passivated interband cascade infrared photodetectors," 2022.

[47] Y. Chen, Z. Xie, J. Huang, Z. Deng, and B. Chen, "High-speed uni-traveling carrier photodiode for 2 μm wavelength application," *Optica*, vol. 6, p. 884, 7 2019.

[48] L. M. Krüger, J. Hillbrand, J. Heidrich, M. Beiser, R. Weih, J. Koeth, C. R. Phillips, B. Schwarz, G. Strasser, and U. Keller, "High-speed interband cascade infrared photodetectors: photo-response saturation by a femtosecond oscillator," *Optics Express*, vol. 29, p. 14087, 4 2021.

[49] D. S. Chemla, A. C. Gossard, P. W. Smith, D. A. Miller, and W. Wiegmann, "Room temperature excitonic nonlinear absorption and refraction in gaas/aigaas multiple quantum well structures," *IEEE Journal of Quantum Electronics*, vol. 20, pp. 265–275, 1984.

[50] D. Burghoff, T.-Y. Kao, N. Han, C. W. I. Chan, X. Cai, Y. Yang, D. J. Hayton, J.-R. Gao, J. L. Reno, and Q. Hu, "Terahertz laser frequency combs," *Nature Photonics*, vol. 8, pp. 462–467, 6 2014.

[51] M. Singleton, P. Jouy, M. Beck, and J. Faist, "Evidence of linear chirp in mid-infrared quantum cascade lasers," *Optica*, vol. 5, p. 948, 8 2018.

[52] J. Hillbrand, A. M. Andrews, H. Detz, G. Strasser, and B. Schwarz, "Coherent injection locking of quantum cascade laser frequency combs," *Nature Photonics*, vol. 13, pp. 101–104, 2 2019.

[53] A. Lardschneider, H. M. Knötig, R. Weih, P. Didier, O. Spitz, J. Koeth, F. Grillot, and B. Schwarz, "Interband cascade infrared photodetectors for high-speed applications," 2022.

[54] O. Spitz, S. Zhao, P. Didier, D. A. Diaz-Thomas, L. Cerutti, A. N. Baranov, H. Knötig, R. Weih, J. Koth, B. Schwarz, and F. Grillot, "Interband cascade technology for next-generation mid-ir communication and quantum applications," pp. 1–2, IEEE, 7 2022.

[55] P. Didier, O. Spitz, L. Cerutti, D. A. Diaz-Thomas, A. N. Baranov, M. Carras, and F. Grillot, "Relative intensity noise and intrinsic properties of rf mounted interband cascade laser," *Applied Physics Letters*, vol. 119, p. 171107, 10 2021.

[56] O. Spitz, P. Didier, L. Durupt, D. A. Diaz-Thomas, A. N. Baranov, L. Cerutti, and F. Grillot, "Free-space communication with directly modulated mid-infrared quantum cascade devices," *IEEE Journal of Selected Topics in Quantum Electronics*, vol. 28, pp. 1–9, 1 2022.

[57] X. Pang, R. Schatz, M. Joharifar, A. Udalcovs, V. Bobrovs, L. Zhang, X. Yu, Y.-T. Sun, G. Maisons, M. Carras, S. Popov, S. Lourdudoss, and O. Ozolins, "Direct modulation and free-space transmissions of up to 6 gbps multilevel signals with a 4.65-μm quantum cascade laser at room temperature," *Journal of Lightwave Technology*, vol. 40, pp. 2370–2377, 4 2022.

[58] A. Bader, F. Rothmayr, N. Khan, F. Hartmann, J. Koeth, and S. Höfling, "Ga-free inas/inassb superlattices for light detection in the mid-infrared spectral region,"